Journal of Catalysis 380 (2019) 352–365

Contents lists available at ScienceDirect

Journal of Catalysis

journal homepage: www.elsevier.com/locate/jcat

# Silicon nitride as a new support for copper catalyst to produce acrolein via selective oxidation of propene with very low $CO_2$ release

Ling-Ling Guo [a,b], Jing Yu [c], Miao Shu [a,b], Lu Shen [d], Rui Si [a,e,*]

[a] Shanghai Institute of Applied Physics, Chinese Academy of Sciences, Shanghai 201800, China
[b] University of Chinese Academy of Science, Beijing 100049, China
[c] Shanghai Institute of Measurement and Testing Technology, Shanghai 200233, China
[d] Division of China, TILON Group Technology Limited, Shanghai 200090, China
[e] Shanghai Synchrotron Radiation Facility, Zhangjiang Laboratory, Shanghai 201204, China

ARTICLE INFO

*Article history:*
Received 10 June 2019
Revised 11 September 2019
Accepted 15 September 2019
Available online 23 October 2019

*Keywords:*
Silicon nitride
Copper-based catalyst
Selective oxidation of propene
Surface hydroxyls
Structure–activity relationship

ABSTRACT

To obtain thermally stable copper-based catalysts with excellent catalytic performance in the selective propene ($C_3H_6$) oxidation reaction, amorphous silicon nitride ($Si_3N_4$) was selected to anchor active copper species using a deposition–precipitation approach followed by air calcination at different temperatures. We found that the thermal treatment temperature remarkably modified the reactivity of the copper catalyst, and the 800 °C-calcined 10 wt% $Cu/Si_3N_4$ showed superior catalytic activity with 24.0% propene conversion and 86.2% acrolein selectivity at 325 °C, featuring a turnover frequency as high as 80.6 $h^{-1}$. With the help of transmission electron microscopy, X-ray absorption fine structure, and in situ X-ray diffraction, we have identified that the larger $Cu_2O$ species account for the highly efficient formation of acrolein at 325 °C. From the CO temperature-programmed reduction results, we have confirmed that the presence of surface copper hydroxyls (Cu–OH) was closely related to the acrolein selectivity, since they favored $CO_2$ generation at the beginning of the reaction. Furthermore, surface copper hydroxyls can be effectively tuned by optimizing the air calcination temperature and thus improve the catalytic activity.



## 1. Introduction

Acrolein is an important chemical intermediate and has been widely used in resin production and organic synthesis [1–4]. The selective oxidation of propene by molecular oxygen to provide high-valued acrolein ($CH_2{=}CH{-}CH_3 + O_2 \rightarrow CH_2{=}CH{-}CHO + H_2O$) has been extensively explored, but is accompanied by several by-products such as acetone, propanal, propylene oxide, and carbon dioxide [5–10]. Since the 1960s, two major catalyst systems for this reaction, bismuth molybdates [11–22] and copper-based catalysts [10,23–35], have been widely investigated. However, how to remarkably improve the acrolein formation and simultaneously minimize the generation of by-products, especially $CO_2$ ($2CH_2{=}CH{-}CH_3 + 9O_2 \rightarrow 6CO_2 + 6H_2O$), is still a major challenge [10,35-38]. On the other hand, copper-based catalysts have been broadly used in selective hydrogenation [39–41], CO oxidation [42,43], the water-gas shift [44,45], methanol dehydrogenation, and many other reactions [46–48]. Among them, oxidized copper materials have also been discovered to be active for selective oxidation of $C_3H_6$ to acrolein [49,50].

In industry, selective oxidation of propene is currently carried out under near-atmospheric pressure at 330 °C or above [32,51]. Thus, much effort has been made in fundamental research to improve both propene conversion and acrolein selectivity for copper-based catalysts [27,29,31]. For instance, Adams and Jennings were the first to report the use of cuprous oxide as a catalyst for selective propene oxidation, obtaining ~10% propene conversion and 60–80% selectivity for acrolein [23,24]. Then Schüth and co-workers applied copper phthalocyanine as a copper precursor that was extremely diluted (below 0.1%) in a silica matrix, which showed moderate activity (conversion 40.1%; selectivity 25.5%) at 475 °C [29]. In 2014, Yang et al. reported vacuum–thermal treated Cu/SBA-15 catalysts resulting in better catalytic stability, while propene tends to be overoxidized to form $CO_2$ with increasing reaction temperature (30% propene conversion and 41% acrolein selectivity at 300 °C) [31]. As a result of these findings, it seemed that there was no good balance between propene conversion at high

* Corresponding author at: Shanghai Institute of Applied Physics, Chinese Academy of Sciences, Shanghai 201800, China.
*E-mail address:* sirui@sinap.ac.cn (R. Si).

https://doi.org/10.1016/j.jcat.2019.09.019
0021-9517/

temperature and acrolein selectivity at low temperature under realistic conditions [52,53].

Other researchers tried to introduce noble metal (Au) into this system to improve the acrolein selectivity to 80–90% at 300 °C or above, but the corresponding conversion of $C_3H_6$ decreased to less than 1% [54,55]. Therefore, effectively enhancing the activity of copper-based catalysts, as well as improving acrolein selectivity under the propene oxidation process conditions (>300 °C, 1 atm), still remains a great challenge. This is probably due to difficulties in rational synthesis of thermally stable catalysts and control of the interactions between copper and support [34,56,57]. Here, the selection of an appropriate support plays a crucial role in achieving high propene conversion and acrolein selectivity for the selective oxidation of $C_3H_6$.

In this paper, we report the successful synthesis of a series of copper-based catalysts anchored on a new type of support, silicon nitride ($Si_3N_4$), which takes multiple advantages [58–63] of (i) its outstanding mechanical and thermal properties at elevated temperatures, which have never been used in the selective propene oxidation reaction; (ii) better thermally and chemically resistant properties than silica, which is usually used as an oxide support in Cu-based catalysts for this reaction. As a result, in this work, we have found that the temperature of thermal treatment on the as-dried samples remarkably tuned their catalytic activity for selective oxidation of propene to produce acrolein. It is very interesting that the acrolein selectivity was significantly promoted over the 800 °C-calcined 10% Cu/$Si_3N_4$ catalyst, achieving 24.0% propene conversion and 86.2% acrolein selectivity (yield > 20%) at 325 °C. The enhanced reactivity can be attributed to the interaction between the copper species and the thermally stable support of the catalyst, as well as the partial elimination of surface copper hydroxyls (Cu–OH) after high-temperature calcination, which favors adsorbing $C_3H_6$ to form $CO_2$ in this reaction.

## 2. Experimental

### 2.1. Catalyst preparation

#### 2.1.1. Materials

Amorphous silicon nitride ($Si_3N_4$, 20 nm, $S_{BET}$ = 67 $m^2$/g, 99.9%), α-silicon nitride (800 nm, 99.9%), and β-silicon nitride (1 μm, 99.9%) were obtained from Shanghai Yao Tian Nano Material Co. SBA-15 ($S_{BET}$ = 600–800 $m^2$/g, >99.5%) was purchased from Nanjing JCNANO Technology Co. Copper nitrate ($Cu(NO_3)_2{\cdot}3H_2O$, 98.0–102.0%), sodium carbonate ($Na_2CO_3$, 99.8%), hydrochloric acid (HCl, 36.0–38.0%), and cuprous oxide ($Cu_2O$, > 90.0%) were purchased from Sinopharm Chemical Reagent Co. and used without purification.

#### 2.1.2. Catalyst preparation

The copper–silicon nitride catalysts were synthesized via a deposition–precipitation method followed by thermal treatment at different temperatures. Typically, 0.38 g $Cu(NO_3)_2{\cdot}3H_2O$ (1.6 mmol) was dissolved in 100 mL Millipore $H_2O$ (>18 MΩ·cm) under vigorous stirring and mixed with 0.9 g $Si_3N_4$ powders. The pH of the Cu precursor and $Si_3N_4$ slurry was adjusted to ~9 by 0.5 M $Na_2CO_3$ aqueous solution and then aged for 4 h at 25 °C. The mixture was centrifuged and washed three times with Millipore water. The as-obtained solid was dried at 75 °C under vacuum for 12 h and then calcined in still air at different temperatures for 4 h (ramp rate: 2 °C/min). The as-prepared 10Cu/$Si_3N_4$ (copper loading amount: 10 wt%) catalyst calcined at $x$°C is denoted as 10Cu/$Si_3N_4$-$x$ ($x$ = 400, 600, 800, or 1000). For comparison, Cu/$Si_3N_4$ was also synthesized with different copper loading amounts calcined at 800 °C and labeled as $y$Cu/$Si_3N_4$-800 ($y$ = 5, 10, 20, and 30), where $y$ is the copper content as a mass percentage ($y$ = [Cu/{Cu + $Si_3N_4$}] × 100%). For the synthesis of 10Cu/SBA-15–800, detailed procedures were the same as for 10Cu/$Si_3N_4$-800, except that the support was different. The $Cu_2O$ particles (10 wt%) were physically mixed with $Si_3N_4$ powders by manual grinding for 20 min and denoted as $b$-$Cu_2O$/$Si_3N_4$. For the leaching of 10Cu/$Si_3N_4$-800, 0.8 g of the powders was washed for 4 h with 100 mL hydrochloric acid aqueous solution (HCl, 5% aq.) at 30 °C under stirring. After being centrifuged and washed in water (pH 7), the sample was dried at 80 °C for 12 h and then air-calcined at 300 °C for 4 h.

### 2.2. Catalyst characterization

#### 2.2.1. Inductively coupled plasma atomic emission spectroscopy

The actual copper concentrations of the catalysts were analyzed by inductively coupled plasma atomic emission spectroscopy (ICP-AES; Optima 5300DV, PerkinElmer). The air-calcined samples (fresh catalysts) were used directly for characterization. First, 0.1 g catalyst (accurate to 0.0001 g) was added to 2 mL hydrofluoric acid under continuous stirring until the powder was dissolved adequately. Second, the as-formed $SiF_4$ was removed via evaporation. Then, almost 3 mL of nitric acid was introduced and the solution was kept slightly boiling for 2 h. Finally, the solution was cooled to nearly 25 °C and diluted for the ICP-AES test.

#### 2.2.2. Nitrogen adsorption–desorption

Nitrogen adsorption–desorption measurements were carried out at 77 K on an ASAP2020-HD88 analyzer (Micromeritics Co.). The air-calcined samples (fresh catalysts) were used directly for characterization. The powder samples were degassed at 250 °C under vacuum (<100 μmHg) for 4 h before being analyzed. The Brunauer–Emmett–Teller (BET) specific surface areas ($S_{BET}$) were calculated based on the data in the relative pressure ($P/P_0$) range between 0.05 and 0.20. The pore size distribution ($d_p$) of the tested sample was calculated from the desorption branch of the isotherms according to the Barrett–Joyner–Halenda (BJH) method.

#### 2.2.3. Transmission electron microscopy

Transmission electron microscopy (TEM) experiments were performed and scanning transmission electron microscopy–energy dispersive spectrometry (STEM-EDS) elemental mapping results were obtained on a FEI Tecnai $G^2$ F20 microscope operating at 200 kV. The fresh (as calcined in air) and used (after 325 °C reaction and exposure to air) catalysts were used for characterization. The tested sample was prepared by suspension in ethanol, and then a drop of this very dilute suspension was cast onto a carbon-film-coated Mo grid. The as-formed sample grid was dried sufficiently before being loaded into the TEM sample holder.

#### 2.2.4. X-ray absorption fine structure

The X-ray absorption fine structure (XAFS) spectra at the Cu $K$-edge ($E_0$ = 8979 eV) were collected at the BL14W1 beamline of the Shanghai Synchrotron Radiation Facility (SSRF) at a typical energy of the storage ring of 3.5 GeV under the "top-up" mode with a constant current of 250 mA. Fresh (as calcined in air) and used (after 325 °C reaction) catalysts were used for characterization. To obtain accurate valence and coordination information on the used catalysts, these samples were transferred into sample tubes and sealed with Ar, after being cooled to room temperature under the reaction gas. Then ca. 30 mg powder was pressed into a solid pellet sealed with Kapton tape before the XAFS test. The XAFS data were recorded in the transmission mode with a Si(1 1 1) monochromator and Oxford ion chambers. The energy was calibrated with the absorption edge of pure Cu foil ($K$-edge, 8979 eV). Athena and Artemis codes were applied to extract the data and fit the profiles. For

X-ray absorption near-edge spectroscopy (XANES), the experimental absorption coefficients as functions of energies, $\mu(E)$, were obtained by background subtraction and normalization procedures and reported as "normalized absorption." On the basis of the normalized XANES profiles, the valences of copper can be acquired via a linear combination fit by means of bulk references (Cu foil for $Cu^0$, $Cu_2O$ for $Cu^+$, and CuO for $Cu^{2+}$). For the extended X-ray absorption fine structure (EXAFS), the Fourier-transformed (FT) data in $R$ space were analyzed using CuO and $Cu_2O$ models for Cu–O and Cu–Cu contributions. The parameters for the description of electronic properties (e.g., correction to the photoelectron energy origin, $E_0$) and local structure environment including $CN$, bond distance ($R$), and Debye–Waller factor around the absorbing atoms were allowed to vary in the fitting process. The fitted ranges for $k$ and $R$ spaces were chosen to be $k$ = 3–12 $Å^{-1}$ with $R$ = 0.8–3.8 Å ($k^3$ weighted).

#### 2.2.5. X-ray diffraction

The ex situ X-ray diffraction (XRD) patterns were determined on a Bruker D8 Advance diffractometer (40 kV, 40 mA) using CuK$\alpha_1$ radiation ($\lambda$ = 1.5406 Å) and a scanning rate of 4°/min. The scanning angle was collected from 10° to 90° using a step of 0.02°. Fresh (as calcined in air) and used (after 325 °C reaction and exposure to air) catalysts were used for characterization. About a 50-mg sample was spread flat on a quartz sample holder for each test. A μm-scale alumina disc was used to calibrate the 2$\theta$ angles, and a quartz sample holder was applied to hold the powder sample. The crystallite size of $Cu/Cu_2O/CuO$ was calculated by the Scherrer equation and the instrumental broadening was corrected by estimating the (1 1 1) peak width of μm-scale alumina. With the least-squares refinement software "LAPOD," cell dimensions from powder data were calculated according to Cohen's method [64,65] with the calibration of 2$\theta$ angle via the (1 1 1) peak of μm-scale alumina.

#### 2.2.6. In situ X-ray diffraction

In situ X-ray diffraction (XRD) was carried out on a PANalytical X'pert3 powder diffractometer (40 kV, 40 mA) equipped with an Anton Paar XRK-900 reaction chamber in the 2θ range 10°–90° (scan rate 4°/min). The fresh (as calcined in air) catalysts were used for characterization. Almost a 15-mg powder sample was loaded into a ceramic sample holder with a diameter of 10 mm and a depth of 1 mm. The tested powders were heated from room temperature to each preset temperature (100, 200, and 300 °C) at a constant rate of 10 °C/min in 5% $H_2$/Ar flow (50 $cm^3 \cdot min^{-1}$) and the corresponding XRD pattern was recorded after each temperature was maintained for 10 min. Then the sample was cooled to room temperature under the $H_2$/Ar flow and the XRD patterns of different atmospheres at 30 °C were collected (5% $H_2$/Ar → He → 1% $C_3H_6$/Ar + 1%$O_2$/$N_2$). Finally, the sample was ramped up to 300 °C for 320 min in a 1% $C_3H_6$/Ar (20 $cm^3 \cdot min^{-1}$) and 1% $O_2$/$N_2$ (20 $cm^3 \cdot min^{-1}$) mixture with XRD pattern collection every 40 min.

#### 2.2.7. Temperature-programmed reduction by hydrogen

Hydrogen temperature-programmed reduction ($H_2$ TPR) was applied to determine the pretreatment temperature under hydrogen. The measurements were carried out on a Micromeritics Autochem II 2920 instrument. Fresh (as calcined in air) catalysts were used for characterization. Prior to the measurement, the catalyst (20–40 mesh, ~100 mg) was pretreated for 30 min in a flow of 5% $O_2$/He (30 mL·$min^{-1}$) at 300 °C (10 °C·$min^{-1}$). The test was carried out from room temperature to 600 °C (10 °C·$min^{-1}$) at a ramp of 10 °C·$min^{-1}$ under 5% $H_2$/Ar (30 mL·$min^{-1}$). A thermal conductivity detector (TCD) was used to detect the changes of hydrogen concentration.

#### 2.2.8. Temperature-programmed reduction by carbon monoxide

Carbon monoxide (CO) TPR experiments using CO as reductant were performed on a mass spectrometer (Tilon GRP Technology Limited LC-D200M). The fresh (as calcined in air) catalysts were used for characterization. The sample (100 mg, 20–40 mesh) was pretreated for 30 min in a flow of 5% $H_2$/Ar (30 mL·$min^{-1}$) at 300 °C, and then cooled down to 30 °C and switched to He (50 mL·$min^{-1}$) for 10 min to purge the reaction system. Finally, the sample was heated from room temperature to 500 °C with a step of 10 °C·$min^{-1}$ under a mixture gas flow of 5% CO/He (20 mL·$min^{-1}$). During the measurement, the signals of He ($m/z$ = 4), $CO_2$ ($m/z$ = 44), $H_2O$ ($m/z$ = 18), CO ($m/z$ = 28), and $H_2$ ($m/z$ = 2) were detected. The reported $CO_2$ and $H_2$ data were normalized by dividing by the corresponding He standard signal ($m/z$ = 4).

#### 2.2.9. Temperature-programmed surface reaction

Temperature-programmed surface reaction (TPSR) measurement of the sample was carried out on a mass spectrometer (Tilon GRP Technology Limited LC-D200M). Fresh (as calcined in air) catalysts were used for characterization. The sample (100 mg, 20–40 mesh) was pretreated for 30 min in 5% $H_2$/Ar (30 mL·$min^{-1}$) or 20% $O_2$/Ar (30 mL·$min^{-1}$) at 300 °C before measurement. After being cooled to room temperature, the sample was ramped to 400 °C with a heating rate of 10 °C·$min^{-1}$ in a continuous $C_3H_6$/$O_2$/He (2.5/2.5/45, 50 mL·$min^{-1}$) mixture gas flow. The signals of He ($m/z$ = 4), $C_3H_5$ ($m/z$ = 41), $O_2$ ($m/z$ = 32), acrolein ($m/z$ = 56), and $CO_2$ ($m/z$ = 44) were tracked. The reported data of $C_3H_6$, $O_2$, $CO_2$, and acrolein were normalized by dividing by the corresponding He standard signal ($m/z$ = 4).

#### 2.2.10. $N_2O$ chemisorption

$N_2O$ chemisorption in a Builder PCSA-1000 instrument was used to determine the Cu dispersion. The fresh (as-calcined in air) catalysts were used for characterization. First of all, the catalyst went through $H_2$ TPR procedure as described above, and the $H_2$ consumption amount ($X$) was corresponded to the total reduction amount of CuO to Cu. Second, the sample was cooled to 35 °C and flushed with helium (30 mL·$min^{-1}$) for 0.5 h, and then flushed with 20% $N_2O/N_2$ gas mixture (30 mL·$min^{-1}$) for 1 h at 35 °C. Finally, the sample was purged with He again for 0.5 h and run the $H_2$ TPR procedure again. The $H_2$ consumption amount ($Y$) was corresponded to the amount of surface $Cu_2O$ reduced to Cu. The Cu dispersion ($D$) was derived as $D = 2Y/X \times 100\%$.

#### 2.2.11. In situ diffuse reflectance infrared Fourier transform spectroscopy

In situ diffuse reflectance infrared Fourier transform spectroscopy (DRIFTS) spectra were collected on a Bruker Vertex 70 FTIR spectrometer equipped with a mercury cadmium telluride (MCT) detector to detect the hydroxyl part in the reduced catalysts with an acquisition time of 40 s. The fresh (as calcined in air) catalysts were used for characterization. Before the test, almost 15 mg of the sample was pretreated in situ in the reaction cell in a5% $H_2$/Ar (30 mL·$min^{-1}$) gas mixture kept at 300 °C for 0.5 h and then cooled to 30 °C in the same atmosphere, followed by pure $N_2$ purging for 20 min.

### 2.3. Catalytic tests

The catalytic performance of the catalysts (100 mg, 40–60 mesh) was determined in a fixed-bed reactor. The gas feed was composed of $C_3H_6$ (2.5 $cm^3 \cdot min^{-1}$), $O_2$ (2.5 $cm^3 \cdot min^{-1}$), and 10% $N_2$/Ar (45 $cm^3 \cdot min^{-1}$) from Jinan Deyang Corporation with a total flow rate of 50 $cm^3 \cdot min^{-1}$. The corresponding space velocity was 30,000 $cm^3 \cdot h^{-1} \cdot g_{cat}^{-1}$. The catalysts were pretreated for 30 min with a 75% $H_2$/Ar (30 $cm^3 \cdot min^{-1}$) gas mixture at 300 °C. Then, once the

reactor was cooled to 30 °C in the reductive atmosphere, 10% $N_2$/Ar was switched and purged for 10 min. Finally, the reaction gases were fed into the reactor, which was heated to the designed temperatures (275, 300, 325, and 350 °C) and the catalytic data were collected at time on stream for 7 h. The outlet gases were detected and analyzed online using a Shimadzu gas chromatograph (GC-9160) every 40 min. A Porapak Q and a 5A molecular sieve-packed column with a thermal conductivity detector (TCD) were used to analyze $CO_2$, $C_3H_6$, and $N_2$. $C_3H_6$, acrolein, propene oxide, aldehyde, propanal, and acetone were analyzed by an AE-FFAP capillary column with a flame ionization detector (FID). The carbon balance for each test was calculated to be 100 ± 3%.

All the calculations, including propene conversion, selectivity ($S_x$) and yield of acrolein and other by-products, and acrolein formation rate ($r_{acrolein}$), are defined for the reaction $aC_3H_6 \rightarrow bC_x$ as follows,

$$\text{conversion}(\%) = \frac{n^{in}_{C_3H_6} - n^{out}_{C_3H_6}}{n^{in}_{C_3H_6}} \times 100,$$

$$S_x(\%) = \frac{\frac{a}{b} n_x}{\sum \frac{a}{b} n_x} \times 100,$$

$$\text{Yield}(\%) = \text{conversion} \times \text{selectivity} \times 100,$$

$$r_{acrolein} = \frac{\text{conversion} \times S_{acrolein} \times n^{in}_{C_3H_6}}{m_{Cu}},$$

$$r_{acrolein} = \frac{\text{conversion} \times S_{acrolein} \times n^{in}_{C_3H_6}}{m_{cat}},$$

$$\text{Turnover frequecy(TOF)} = \frac{\text{conversion} \times S_{acrolein} \times n^{in}_{C_3H_6}}{D \times n_{Cu}},$$

where $n_x$ is the partial moles of the analyzed products in this reaction (aldehyde, propane, acetone, propene oxide, acrolein, and $CO_2$).

## 3. Results and discussion

### 3.1. Structural characterization of fresh copper–silicon nitride catalysts

Table 1 summarizes the textural properties of copper–silicon nitride catalysts after they are calcined at different temperatures. The bulk concentrations of copper ($Cu_{bulk}$) were determined by ICP-AES and the value of 10Cu/$Si_3N_4$ was close to the designated number when the sample was calcined at a low temperature of 400 °C. However, when the calcination temperature was increased to 600–1000 °C, the experimental values gradually decreased, which was ascribed to the partial oxidation of $Si_3N_4$ to $SiO_2$ at the elevated air-calcination temperatures. On the other hand, we applied $H_2$ TPR experiments to investigate the reducibility of these catalysts. As shown in Fig. S1 in the Supplemental Information, a single broad peak was detected in the region of 150–350 °C for each sample. With the increase of air-calcination temperature, the center of the reduction peak shifts to a higher temperature, indicating a larger Cu(II) component formed on the surface of the silicon nitride support or a strengthened interaction between the metal (Cu) and support ($Si_3N_4$). Furthermore, the $H_2$ consumption rates in this temperature range are equal to the theoretical surface oxygen numbers in this work, implying the complete reduction of Cu(II) to Cu(0); see Table 1 [66].

As shown in the XRD patterns (Fig. 1a), a broad weak peak was detected at about 23° for 10Cu/$Si_3N_4$ calcined at 800 °C, corresponding to the generation of amorphous $SiO_2$, and became stronger with increased calcination temperature. However, the pattern is complicated for 10Cu/$Si_3N_4$-1000, with other phases appearing, including α-$SiO_2$ (PDF#01-083-2466), which was caused by the severe decomposition of $Si_3N_4$ support. Furthermore, we analyzed the oxidation degree of $Si_3N_4$ (oxidized to $SiO_2$) for these samples on the basis of the ICP-AES data (Fig. S2). Remarkably, the oxidation degree of $Si_3N_4$ exceeded 60% at 1000 °C, confirming that the structure of 10Cu/$Si_3N_4$-1000 was dramatically changed. However, 10Cu/$Si_3N_4$-800 maintained its intrinsic structure with a relatively lower oxidation degree of 29% in experiments. For the 800 °C-calcined 10Cu/SBA-15, the original structure of the SBA-15 support was completely converted into α-$SiO_2$ (Fig. S3), indicating its relatively poorer thermal stability than that of $Si_3N_4$. On the other hand, no Cu/$Cu_2O$/CuO characteristic peaks were observed for 10Cu/$Si_3N_4$-400 in Fig. 1a, indicating the formation of amorphous copper species. The diffraction peaks assigned to CuO (PDF#00-045-0937) were clearly determined and become stronger, with a calculated average grain size from 27 to 33 nm (see Table 1), when the calcination temperature increased from 600 to 800 °C. Furthermore, as shown in Fig. 1b, the peak intensities of CuO in different samples are almost identical when $Cu_{bulk}$ reaches 10 wt% under the same testing conditions (power of X-ray source, thickness of sample loading, etc.), revealing their similar crystallinity. In addition, we applied $N_2O$ titration to calculate the Cu dispersion ($D$) of the catalyst, which was directly associated with the surface-active sites during the reaction (Fig. S4 and Table 1). The Cu dispersion of 10Cu/$Si_3N_4$-400 was 45.2%, much higher than that of 10Cu/$Si_3N_4$-800 (10.8%), 20Cu/$Si_3N_4$-800 (11.9%), or 10Cu/SBA-15-800 (12.3%), further confirming the smaller size of copper species distributed on the surface of the former, while larger copper species existed in the latter [35]. Besides the amorphous $Si_3N_4$, the

**Table 1**
Physical properties of copper–silicon nitride samples.

| Sample | $Cu_{bulk}$ (wt.%)[a] | $H_2$ consumption (mmol·g$^{-1}$) | | $S_{BET}$ ($m^2g^{-1}$) | $d_p$ (nm) | $V_p$ ($cm^3g^{-1}$) | $D_{XRD}$ (nm)[d] | $D_{TEM}$ (nm)[e] | Cu dispersion (%)[f] | $D_{XRD}$ (nm)[g] |
|---|---|---|---|---|---|---|---|---|---|---|
| | | Experimental[b] | Theoretical[c] | | | | | | | |
| $Si_3N_4$ | – | – | – | 67 | 16 | 0.17 | – | – | – | – |
| 10Cu/$Si_3N_4$-400 | 10.0 | 1.56 | 1.57 | 76 | 30 | 0.49 | – | 3.6 ± 1.0 | 45.2 | 4.9 |
| 10Cu/$Si_3N_4$-600 | 9.7 | 1. 53 | 1.53 | 94 | 23 | 0.49 | 27 | – | – | 26 |
| 10Cu/$Si_3N_4$-800 | 9.3 | 1.46 | 1.46 | 60 | 26 | 0.31 | 33 | 38 ± 37 | 10.8 | 35 |
| 10Cu/$Si_3N_4$-1000 | 8.6 | 1.35 | 1.35 | 4 | 60 | 0.02 | 32 | – | – | 36 |

[a] Determined by ICP-AES.
[b] Integrated $H_2$ TPR peak area from room temperature to 500 °C.
[c] Calculated by assuming the complete reduction of CuO to Cu.
[d] Particle size of as-calcined samples calculated from the XRD data by the Scherrer equation.
[e] Statistic from over 100 particles in TEM images.
[f] Determined by $N_2O$ titration.
[g] Particle size of 325 °C used samples calculated from the XRD data by the Scherrer equation.

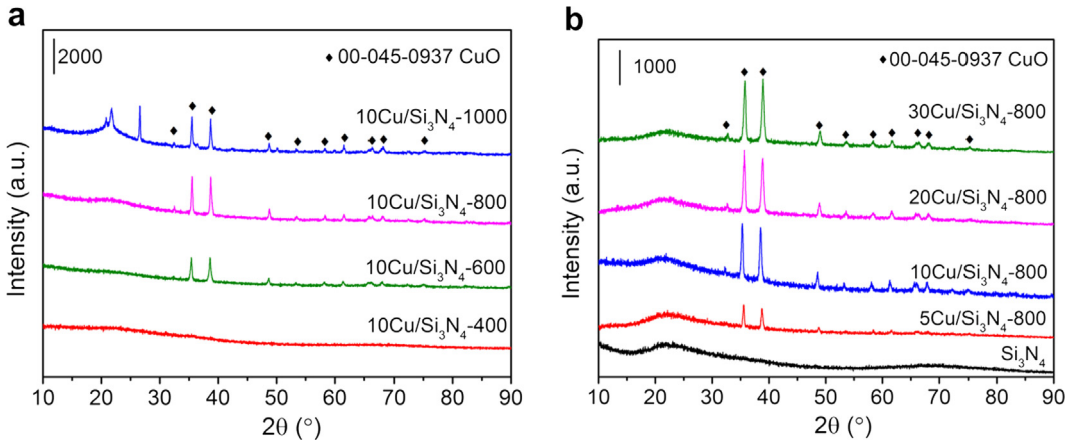


**Fig. 1.** XRD patterns of fresh copper–silicon nitride catalysts: (a) 10 wt% Cu with different calcination temperatures; (b) calcined at 800 °C with different copper concentrations.

crystallized $Si_3N_4$, including α-$Si_3N_4$ and β-$Si_3N_4$, were also investigated for the present copper catalysts (10Cu/α-$Si_3N_4$-800 and 10Cu/β-$Si_3N_4$-800). The diffraction peaks of CuO, along with the support (α-$Si_3N_4$ or β-$Si_3N_4$), were clearly observed, giving a hint of the excellent thermal stability of these $Si_3N_4$ materials (Fig. S5).

Nitrogen absorption measurements were carried out to detect the textural properties of as-calcined catalysts. The adsorption/desorption isotherms and the corresponding pore-size distribution on typical samples ($Si_3N_4$, 10Cu/$Si_3N_4$-400, 10Cu/$Si_3N_4$-600, 10Cu/$Si_3N_4$-800, and 10Cu/$Si_3N_4$-1000) are shown in Fig. 2a and 2b, respectively. These curves display a typical type IV isotherm with an H3 hysteresis loop in the $P/P_0$ range 0.8–1.0, indicating textural porosity. Particularly, 10Cu/$Si_3N_4$-1000 showed a very low value of BET surface area (4 $m^2$ $g^{-1}$) compared with all the other samples, which was caused by the collapse of its structure at the elevated calcination temperature. Table 1 shows that the average pore sizes ($d_p$) of 23–60 nm for copper-silicon nitride samples are obviously larger than that of the pure $Si_3N_4$ support (16 nm). Furthermore, the BJH pore volumes ($V_p$) gradually decrease with air-calcination temperatures above 600 °C (see Table 1). These results demonstrate that while the average pore sizes were largely maintained, the surface areas and pore volumes of 10Cu/$Si_3N_4$ dropped continuously after high-temperature air calcination.

The morphology of as-calcined copper–silicon nitride samples was investigated by TEM. For 10Cu/$Si_3N_4$-400, the smaller (<5 nm) nanoparticles are uniformly distributed on the surface of $Si_3N_4$ with an average size of 3.6 ± 1.0 nm, and no aggregated copper species were observed (Fig. 3a–d). Fig. 3c verifies the copper dispersion on the surface of $Si_3N_4$ with the help of STEM-EDS mappings. But for 10Cu/$Si_3N_4$-800, Fig. 3e–g show unevenly large (20 nm and above) copper species, revealing the growth of copper during high-temperature (800 °C) air calcination. Based on the TEM data, we can obtain the average particle size for copper component as 38 nm with a rather wide distribution (Fig. 3h), in accordance with the XRD results.

To investigate the electronic structure (oxidation state) and local coordination structure (distance and coordination number) of the copper species supported on $Si_3N_4$, we conducted XAFS measurements. The XANES profiles of the as-calcined 10Cu/$Si_3N_4$-400, 10Cu/$Si_3N_4$-600, 10Cu/$Si_3N_4$-800, and 10Cu/$Si_3N_4$-1000 in Fig. 4a show edge jump energy similar to that of the CuO reference in the region 8980–8990 eV. This implies that the present copper species were in the oxidized $Cu^{2+}$ state for these samples. Even 10Cu/$Si_3N_4$-400 exhibits a different edge shape. As shown in Fig. 4b, the related EXAFS spectrum for 10Cu/$Si_3N_4$-400 displays a dominant peak at approximately 1.95 Å derived from the first shell of Cu—O, plus a secondary Cu—Cu shell at a distance of ca. 2.94 Å, corresponding to the Cu—O—Cu structure in the CuO model (see Table 2). Compared with the bulk CuO reference, the lower intensity of the Cu—Cu shell in 10Cu/$Si_3N_4$-400 indicates its lower crystallinity. For other samples such as 10Cu/$Si_3N_4$-600, 10Cu/$Si_3N_4$-800, and 10Cu/$Si_3N_4$-1000, two additional Cu—Cu characteristic peaks are present at distances of 3.10 and 3.85 Å (Fig. 4b and Table 2), which can be assigned to the highly crystallized CuO structure in these

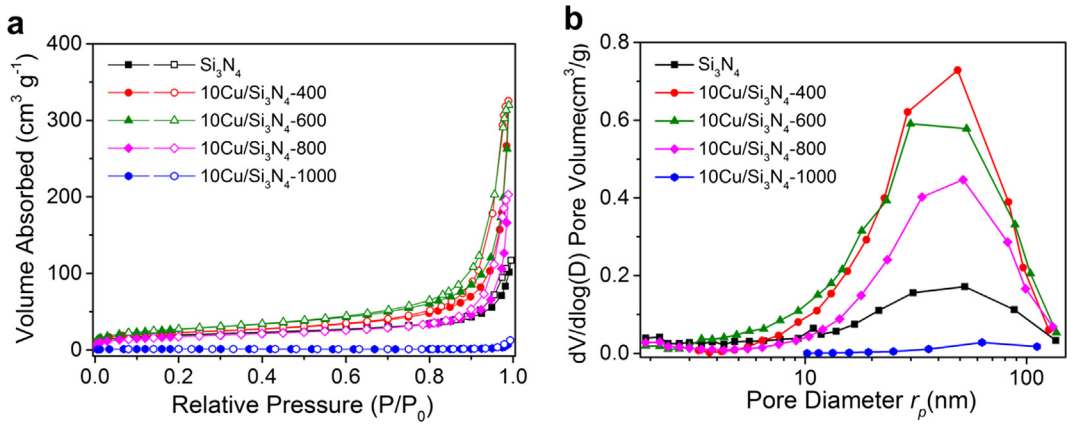


**Fig. 2.** Nitrogen adsorption–desorption curves of fresh copper–silicon nitride catalysts: (a) adsorption–desorption isotherm; (b) BJH pore-size distribution.

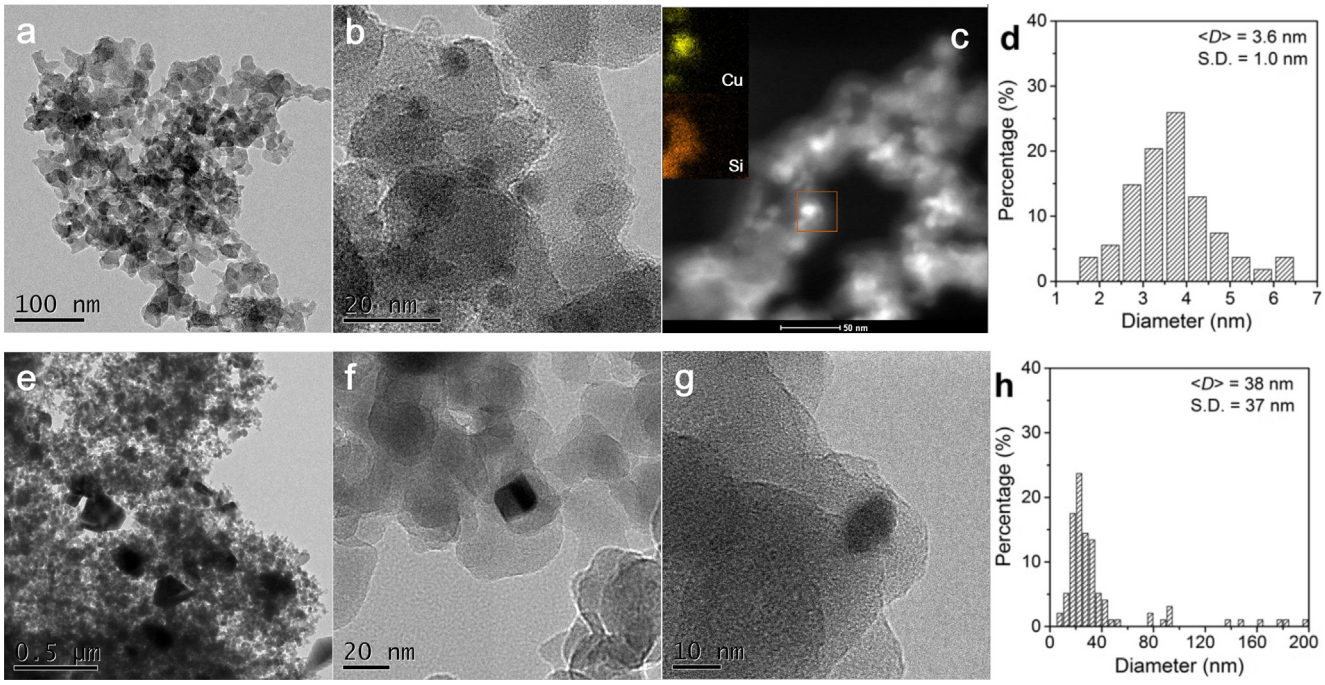


**Fig. 3.** TEM images (a, b, e–g), the related STEM-EDS mapping results (c), and particle-size histograms for copper species (d, h) in fresh copper–silicon nitride catalysts: (a–d) 10Cu/$Si_3N_4$-400; (e–h) 10Cu/$Si_3N_4$-800.

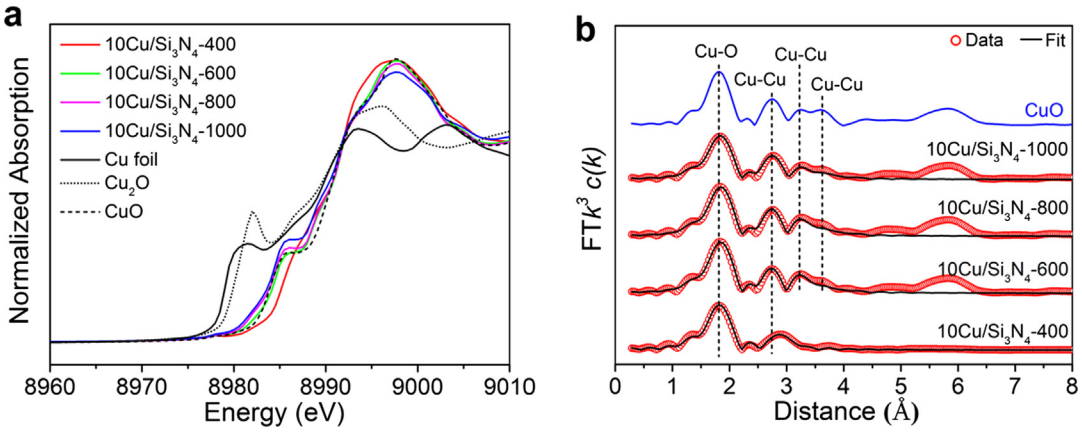


**Fig. 4.** Cu *K*-edge XANES profiles (a) and EXAFS fitting results in *R* space (b) of fresh copper–silicon nitride samples.

**Table 2**
Cu *K*-edge EXAFS fitting results (*R*: distance; CN: coordination number; $\sigma^2$: Debye–Waller factor;[a] $\triangle E_0$: inner potential correction[b]) of as-calcined copper–silicon nitride samples.

| Sample | Cu—O | | Cu—Cu | | Cu—Cu | | Cu—Cu | |
|---|---|---|---|---|---|---|---|---|
| | *R* (Å) | CN | *R* (Å) | CN | *R* (Å) | CN | *R* (Å) | CN |
| CuO | 1.948 | 4 | 2.884 | 4 | 3.115 | 6 | 3.727 | 2 |
| 10Cu/$Si_3N_4$-400 | 1.95 ± 0.01 | 3.6 ± 0.1 | 2.94 ± 0.01 | 1.3 ± 0.2 | – | – | – | – |
| 10Cu/$Si_3N_6$-600 | 1.95 ± 0.01 | 4.2 ± 0.2 | 2.91 ± 0.01 | 3.9 ± 0.5 | 3.10 ± 0.01 | 4.2 ± 0.6 | 3.85 ± 0.03 | 1.2 ± 0.5 |
| 10Cu/$Si_3N_4$-800 | 1.95 ± 0.01 | 4.1 ± 0.2 | 2.90 ± 0.01 | 4.2 ± 0.4 | 3.10 ± 0.01 | 4.3 ± 0.5 | 3.85 ± 0.03 | 1.3 ± 0.4 |
| 10Cu/$Si_3N_4$-1000 | 1.95 ± 0.01 | 3.6 ± 0.2 | 2.91 ± 0.01 | 3.5 ± 0.4 | 3.10 ± 0.01 | 3.3 ± 0.5 | 3.84 ± 0.03 | 1.0 ± 0.5 |

[a] $\sigma^2$ = 0.0045 Å$^2$ (Cu—O) or 0.007 Å$^2$ (Cu—Cu) for all analyzed samples.
[b] $\Delta E_0$ = 11.8 eV for all analyzed samples.

high-temperature air-calcined catalysts. These findings are in good agreement with the XRD (Fig. 1a) and TEM (Fig. 3) results.

As discussed above, we found that the copper species can be anchored successfully onto the silicon nitride support via a deposition–precipitation method, and the particle size of obtained copper catalysts can be tuned effectively by selecting the appropriate air-calcination temperature. With the help of TEM, XRD, XANES, and EXAFS analyses, we have confirmed that the amorphous copper oxide species were highly dispersed on the $Si_3N_4$ support for 10Cu/$Si_3N_4$-400, while the CuO crystals with larger size

appeared for these copper–silicon nitride catalysts calcined at elevated temperature.

### 3.2. Catalytic performance

To explore the catalytic performance of copper–silicon nitride catalysts, the selective oxidation of propene to acrolein at 275–350 °C has been carefully evaluated (see Table S1). All the tested samples were pretreated at 300 °C in a reducing atmosphere (75% $H_2/N_2$) for 30 min before the catalytic measurement. The reported data on conversion of propene and selectivity for acrolein or other by-products were averaged from the relatively stable experimental points from 160 to 320 min. As shown in Fig. 5, acrolein and $CO_2$ are the dominant products (>98%), and the other by-products can be neglected. Fig. 5a presents the propene conversion and selectivity of each product on the $Cu/Si_3N_4$ catalysts with different Cu loading amounts (5, 10, 20, and 30 wt%) at 325 °C (see Fig. S6). Although the acrolein selectivity is located in a very narrow region of 82.7–87.6%, the propene conversion of $10Cu/Si_3N_4$-800 shows a significantly higher value (24.0%) than for all the other samples calcined at 800 °C (9.0–11.1%). On the other hand, reaction temperature also plays an important role in the catalytic performance of these copper–silicon nitride catalysts. Fig. 5b and Fig. S7 show that the acrolein selectivity increased

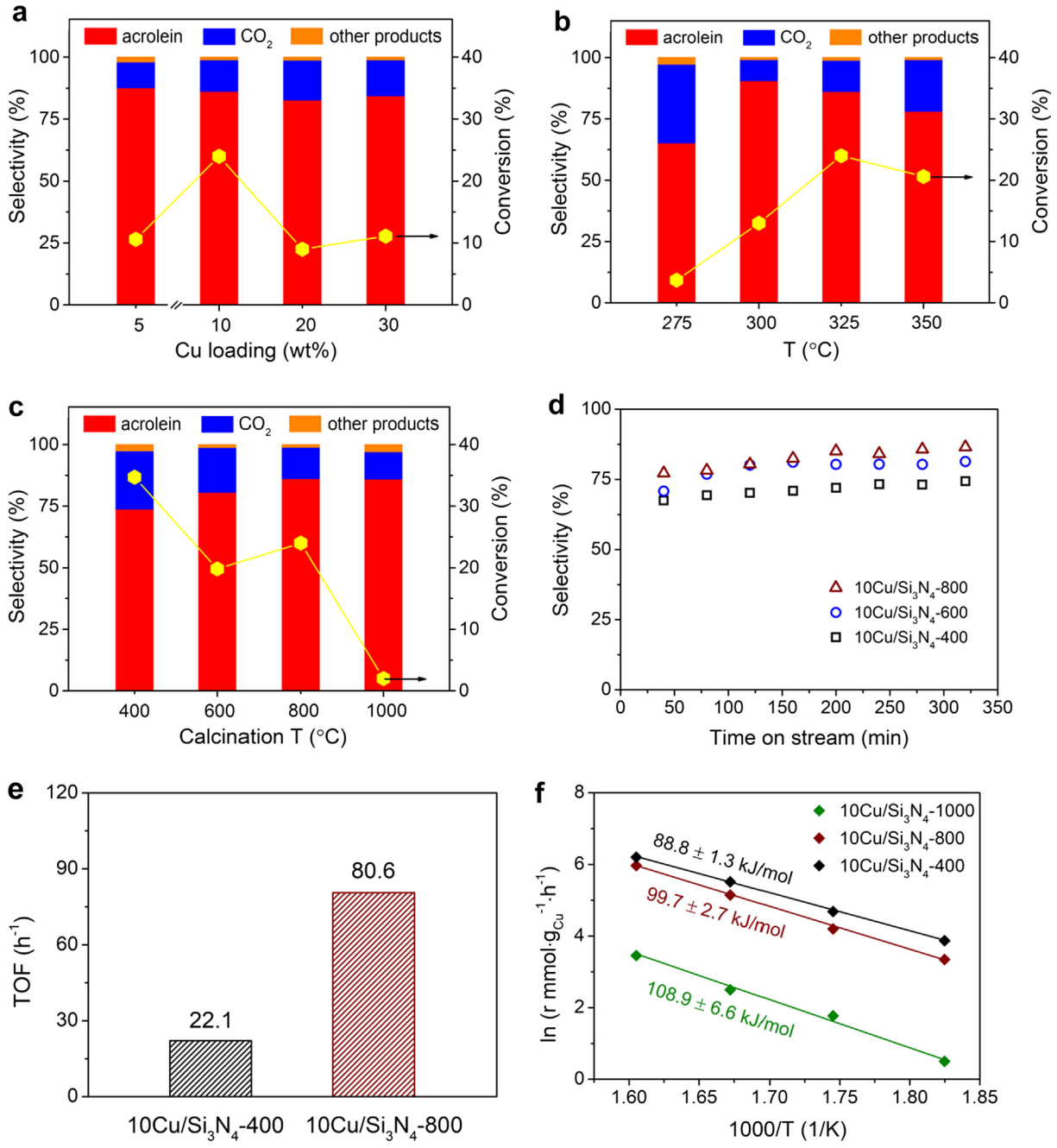


**Fig. 5.** Catalytic performance of copper–silicon nitride catalysts: (a) different Cu loading amounts at 325 °C, (b) different reaction temperatures for $10Cu/Si_3N_4$-800, and (c) different air-calcination temperatures for $10Cu/Si_3N_4$ at 325 °C. (d) Comparison of acrolein selectivities at similar propene conversions for different space velocities ($10Cu/Si_3N_4$-400, 50,000 $cm^3 \cdot h^{-1} \cdot g_{cat}^{-1}$; $10Cu/Si_3N_4$-600, 30,000 $cm^3 \cdot h^{-1} \cdot g_{cat}^{-1}$; $10Cu/Si_3N_4$-800, 35,700 $cm^3 \cdot h^{-1} \cdot g_{cat}^{-1}$) at 325 °C. (e) TOF values for acrolein formation at 325 °C. (f) Apparent activation energy ($E_a$). Reaction conditions: 100 mg catalyst, $C_3H_6:O_2:N_2/Ar$ = 5:5:90, 50 mL·min$^{-1}$.

rapidly from 65.2% (275 °C) to 90.6% (300 °C), and then slowly decreased to 78.1% (350 °C). However, the propene conversion was proportionally raised in the region 275–325 °C (3.7%→13.0%→24.0%) and then dropped slightly to 20.6% at 350 °C. Generally speaking, the catalytic activity on the current copper–silicon nitride catalyst was greatly modified when the Cu loadings and reaction temperatures were changed. Among the catalysts, 10Cu/$Si_3N_4$-800 exhibited superior catalytic activity for the reaction of selective propene oxidation to acrolein at 325 °C.

Furthermore, we investigated the effect of air-calcination temperature (400, 600, 800, and 1000 °C) of copper–silicon nitride samples on the catalytic activity for selective oxidation of propene (see Fig. S8). In Fig. 5c, kept at 325 °C, the acrolein selectivity was increased monotonically from 73.8% (10Cu/$Si_3N_4$-400) to 86.2% (10Cu/$Si_3N_4$-800), while the related propene conversion was decreased from 34.7% (10Cu/$Si_3N_4$-400) to 19.8% (10Cu/$Si_3N_4$-600) and then partially recovered to 24.0% (10Cu/$Si_3N_4$-800). To rigorously compare the acrolein selectivity on these samples, the catalytic tests were performed at similar propene conversion (~20%) by regulating the space velocity. As shown in Fig. 5d, the selectivity of acrolein could be ordered as 10Cu/$Si_3N_4$-400 < 10Cu/$Si_3N_4$-600 < 10Cu/$Si_3N_4$-800 when reacted at 325 °C, especially for a long time period, indicating that the acrolein selectivity can be optimized effectively by tuning the calcined temperatures of copper–silicon nitride catalysts. In particular, the 10Cu/$Si_3N_4$-800 exhibits promoted catalytic activity for selective oxidation of propene to acrolein with a superhigh selectivity of 86.2% for acrolein (<13% for $CO_2$) at 325 °C, which is higher than those of all the previously reported copper-based catalysts [10,23–35]. In addition, the acrolein formation rate of 10Cu/$Si_3N_4$-800 reaches 136.9 mmol·$h^{-1}$·$g_{Cu}^{-1}$ at 325 °C, which is higher than those from the very active 1 wt% Cu/$SiO_2$ (57.1 mmol·$h^{-1}$·$g_{Cu}^{-1}$, 325 °C) [27] and 5 wt% Cu/$SiO_2$ (24.9 mmol·$h^{-1}$·$g_{Cu}^{-1}$, 325 °C) [27] at similar reaction temperatures, and even higher than the very high-temperature-reacted CuPc/SBA-15 catalyst (90.5 mmol·$h^{-1}$·$g_{Cu}^{-1}$ at 475 °C) [29] (Fig. S9), revealing the remarkable catalytic performance of our 10Cu/$Si_3N_4$-800 in the selective oxidation of propene to acrolein reaction.

Table 3 summarizes the results of propene conversion and acrolein selectivity, as well as the formation rate of acrolein, over these copper–silicon nitride catalysts. For comparison, pure $Si_3N_4$ was applied to this reaction at 325 °C and did not convert any propene (Fig. S10). The acrolein formation rates normalized by copper weight in Table 3 show that Cu efficiency is nearly identical between 5 wt% (131.0 mmol·$h^{-1}$·$g_{Cu}^{-1}$) and 10 wt% (136.9 mmol·$h^{-1}$·$g_{Cu}^{-1}$), and then decreases severely for 20 wt% (24.0 mmol·$h^{-1}$·$g_{Cu}^{-1}$) and 30 wt% (21.5 mmol·$h^{-1}$·$g_{Cu}^{-1}$), confirming that 10 wt% Cu is optimized in our study. To gain further insight into the reactivity of the catalyst, the turnover frequency (TOF) of acrolein was estimated on the basis of the copper dispersion using $N_2O$ titration. In Fig. 5e and Table 3, it is clear that 10Cu/$Si_3N_4$-800 attained the highest TOF value of 80.6 $h^{-1}$, significantly higher than those of 10Cu/$Si_3N_4$-400 (22.1 $h^{-1}$), 20Cu/$Si_3N_4$-800 (12.8 $h^{-1}$), and 10Cu/SBA-15–800 (2.4 $h^{-1}$). Meanwhile, the acrolein formation rate and the TOF value increased sharply with the reaction temperature from 275 to 325 °C, indicating that a higher reaction temperature is more beneficial for copper–silicon nitride catalysts air-calcined at 800 °C. When normalized by catalyst weight, the acrolein formation rates of 10Cu/$Si_3N_4$ in Table 3 shows a severe decline (15.7 mmol·$h^{-1}$·$g_{cat}^{-1}$ → 1.1 mmol·$h^{-1}$·$g_{cat}^{-1}$) when the pretreated temperature increased from 400 to 1000 °C, except that the 800 °C air-calcined catalyst exhibited an enhanced acrolein formation rate of 12.7 mmol·$h^{-1}$·$g_{cat}^{-1}$, which is much higher than not only the other loading catalysts calcined at the same temperature, but also the reported values in the literature [27,29]. Particularly, for 10Cu/$Si_3N_4$-1000, either the acrolein formation rate of 12.8 mmol·$h^{-1}$·$g_{Cu}^{-1}$ or 1.1 mmol·$h^{-1}$·$g_{cat}^{-1}$ or the TOF of 7.5 $h^{-1}$ was nearly an order of magnitude lower than that of 10Cu/$Si_3N_4$-800, which was probably caused by the significant structural changes of the $Si_3N_4$ support after air calcination at 1000 °C (Fig. 1a and S2). In Fig. 5f, the apparent activation energies ($E_a$) calculated from the Arrhenius plots at low propene conversions (<15%) were 88.8 ± 1.3, 99.7 ± 2.7, and 108.9 ± 6.6 kJ·$mol^{-1}$ for 10Cu/$Si_3N_4$-400, 10Cu/$Si_3N_4$-800, and 10Cu/$Si_3N_4$-1000, respectively, revealing that the larger copper species supported on silicon nitride (10Cu/$Si_3N_4$-800) require a slightly higher barrier energy to activate the reaction than the smaller 10Cu/$Si_3N_4$-400 catalyst. The 10Cu/$Si_3N_4$-800 and 10Cu/$Si_3N_4$-1000, which possess similar average sizes of copper species (~33 nm), exhibited a slightly different apparent activation energy, implying that the superior catalytic performance lies in the maintaining of such an amorphous, partially oxidized $Si_3N_4$ surface, which probably affected the activation of propene or $O_2$ in this reaction. Moreover, in order to explore the effect of crystallinity of the support on catalytic activity, copper catalysts on α-$Si_3N_4$ and β-$Si_3N_4$ air-calcined at 800 °C were evaluated at 325 °C. As shown in Fig. S11, compared with the amorphous $Si_3N_4$-supported sample (Fig. S6b), the acrolein selectivity of these catalysts (10Cu/$Si_3N_4$-800 with amorphous $Si_3N_4$, α-$Si_3N_4$, and

**Table 3**
Catalytic performance for selective oxidation of propene to acrolein over copper–silicon nitride catalysts.

| Sample | $T$ (°C) | Conversion (%) | $S_{acrolein}$ (%) | Rate (mmol·$h^{-1}$·$g_{Cu}^{-1}$) | Rate (mmol·$h^{-1}$·$g_{cat}^{-1}$) | TOF ($h^{-1}$) |
|---|---|---|---|---|---|---|
| $Si_3N_4$ | 325 | 0 | 0 | 0 | 0 | 0 |
| 10Cu/$Si_3N_4$-400 | 325 | 34.7 | 73.8 | 157.5 | 15.7 | 22.1 |
| 10Cu/$Si_3N_4$-600 | 325 | 19.8 | 80.6 | 100.6 | 9.8 | 59.1[a] |
| 10Cu/$Si_3N_4$-800 | 275 | 3.7 | 65.2 | 16.2 | 1.5 | 9.5 |
| 10Cu/$Si_3N_4$-800 | 300 | 13.0 | 90.6 | 77.6 | 7.2 | 45.6 |
| 10Cu/$Si_3N_4$-800 | 325 | 24.0 | 86.2 | 136.9 | 12.7 | 80.6 |
| 10Cu/$Si_3N_4$-800 | 350 | 20.6 | 78.1 | 106.7 | 9.9 | 62.7 |
| 10Cu/$Si_3N_4$-1000 | 325 | 2.0 | 86.0 | 12.8 | 1.1 | 7.5[a] |
| 5Cu/$Si_3N_4$-800 | 325 | 10.6 | 87.6 | 131.0 | 5.7 | – |
| 20Cu/$Si_3N_4$-800 | 325 | 9.0 | 82.7 | 24.0 | 4.6 | 12.8 |
| 30Cu/$Si_3N_4$-800 | 325 | 11.1 | 84.4 | 21.5 | 5.7 | 12.6[a] |
| 10Cu/α-$Si_3N_4$-800 | 325 | 13.8 | 83.8 | 70.9 | 7.1 | 41.7[a] |
| 10Cu/β-$Si_3N_4$-800 | 325 | 6.0 | 85.6 | 31.5 | 3.2 | 18.5[a] |
| 10Cu/SBA-15-800 | 325 | 1.9 | 38.3 | 4.5 | 0.4 | 2.4 |
| CuPc/SBA-15[(Ref.29)] | 475 | 14.9 | 59.0 | 90.5 | 0.3 | – |
| 1 wt% Cu/$SiO_2$[(Ref.27)] | 325 | 2.3 | 40.5 | 57.1 | 0.6 | – |
| 5 wt% Cu/$SiO_2$[(Ref.27)] | 325 | 7.5 | 27.1 | 24.9 | 1.2 | – |

*Note:* Reaction conditions: 100 mg catalyst, $C_3H_6$:$O_2$:$N_2$/Ar = 5:5:90, 50 mL·$min^{-1}$.
[a] The values were estimated based on the copper dispersion of 10Cu/$Si_3N_4$-800, which exhibited similar average size, according to XRD results.

β-$Si_3N_4$) was almost the same, while the propene conversion decreased in the order 10Cu/$Si_3N_4$-800 (24.0%) > 10Cu/α-$Si_3N_4$-800 (13.8%) > 10Cu/β-$Si_3N_4$-800 (6.0%), confirming that the amorphous $Si_3N_4$ support was a promising candidate in this reaction.

To highlight the superiority of the amorphous silicon nitride support to this higher-temperature selective oxidation reaction, a conventional SBA-15 was selected as a support for copper (10Cu/SBA-15-800) and was prepared via a similar procedure. The stability tests of 10Cu/SBA-15-800, 10Cu/$Si_3N_4$-800, and 10Cu/$Si_3N_4$-400 were conducted at 325 °C (see Fig. 6 and S12), and the average propene conversion for 10Cu/SBA-15-800 was just 1.6% at 325 °C in the initial 400 min, which was much less than that for 10Cu/$Si_3N_4$-800 (24%) and 10Cu/$Si_3N_4$-400 (35%). This can be attributed to the structural collapse of SBA-15 after air calcination at 800 °C (Fig. S3), while the structure of the $Si_3N_4$ support was maintained (Fig. 1a). Moreover, 10Cu/SBA-15-800 featured a very long induction period: the selectivity for acrolein was gradually increased from 22 to 40% in almost 400 min, while the values for 10Cu/$Si_3N_4$-400 and 10Cu/$Si_3N_4$-800 were almost twice as high, and displayed a slowly rising tendency in approximately 1200 min. Notably, the propene conversion of 10Cu/$Si_3N_4$-400 was higher than that of 10Cu/$Si_3N_4$-800 at the beginning of the reaction, but declined linearly throughout the whole reaction process, while the propene conversion of 10Cu/$Si_3N_4$-800 nearly leveled off after 400 min, revealing the excellent stability of the larger copper–silicon nitride catalyst after air calcination at 800 °C for acrolein formation via selective oxidation of propene.

### 3.3. Structural characterization of used copper–silicon nitride catalysts

The XRD patterns of the used copper–silicon nitride catalysts (Fig. 7 and S13) show obvious diffraction peaks at 36.52°, 42.42°, 61.55°, and 73.74°, which can be assigned to the (1 1 1), (2 0 0), (2 2 0), and (3 1 1) planes of $Cu_2O$ (PDF#00-005-0667), respectively. This indicates that the CuO species in fresh catalysts have been transformed to the $Cu_2O$ component during the selective oxidation of propene. Similar structural transformations were detected in 10Cu/α-$Si_3N_4$-800, 10Cu/β-$Si_3N_4$-800, and 10Cu/SBA-15-800 (Figs. S14 and S15). Furthermore, we have calculated the average grain sizes of $Cu_2O$ in these samples by using the Scherrer equation (see Table 1). Clearly, the diffraction peaks became sharper with increased air-calcination temperature or reaction temperature, revealing the formation of $Cu_2O$ (Fig. 7 and Table 1). Unlike the 325 °C-used 10Cu/$Si_3N_4$ samples, a fraction of CuO was observed in both 350 °C- and 275 °C-used 10Cu/$Si_3N_4$-800 (Fig. 7b) and 20Cu/$Si_3N_4$-800 or 30Cu/$Si_3N_4$-800 (Fig. S13), implying that part of the $Cu_2O$ species could be overoxidized to the CuO structure under these reaction conditions. Thus, the existence of this CuO phase could lead to a decreased propene conversion or acrolein formation rate (see Table 3, Figs. S6 and S7).

Fig. 8 shows TEM images of used copper–silicon nitride samples. For 10Cu/$Si_3N_4$-400, the uniform copper species with an average size less than 5 nm were still highly dispersed on the surface of the $Si_3N_4$ support (Fig. 8a–8d), while nonuniform larger copper species were observed for 10Cu/$Si_3N_4$-800 (Fig. 8e, 8f).

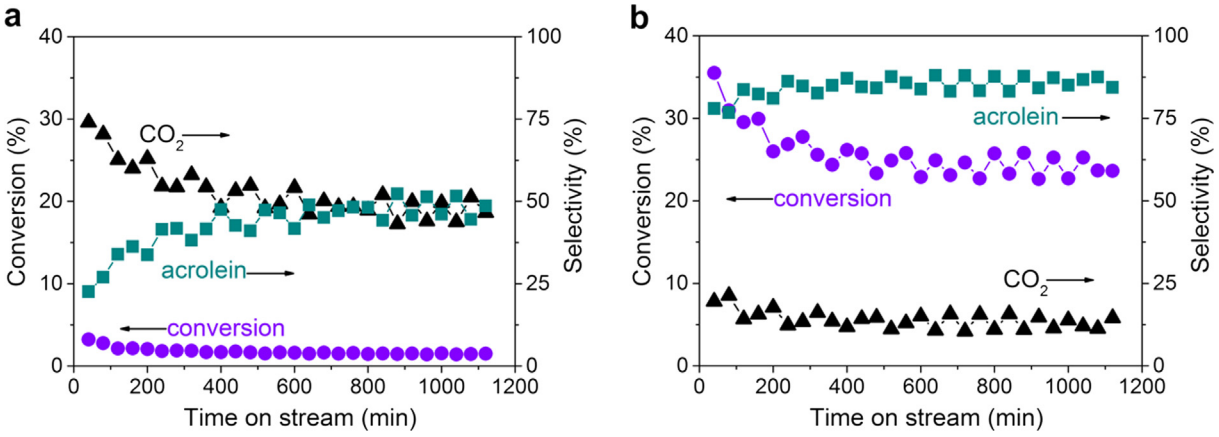


**Fig. 6.** Stability test of (a) 10Cu/SBA-15-800 and (b) 10Cu/$Si_3N_4$-800 at 325 °C. Reaction conditions: 100 mg catalyst, $C_3H_6$:$O_2$:$N_2$/Ar = 5:5:90, 50 mL·min$^{-1}$.

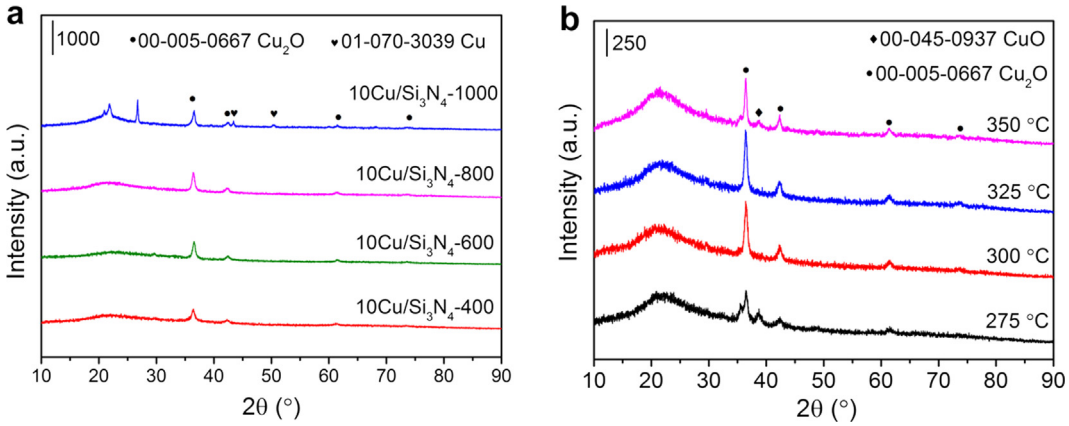


**Fig. 7.** XRD patterns of used copper–silicon nitride catalysts: (a) different 10Cu/$Si_3N_4$ samples after reaction at 325 °C; (b) 10Cu/$Si_3N_4$-800 after reaction at different temperatures.

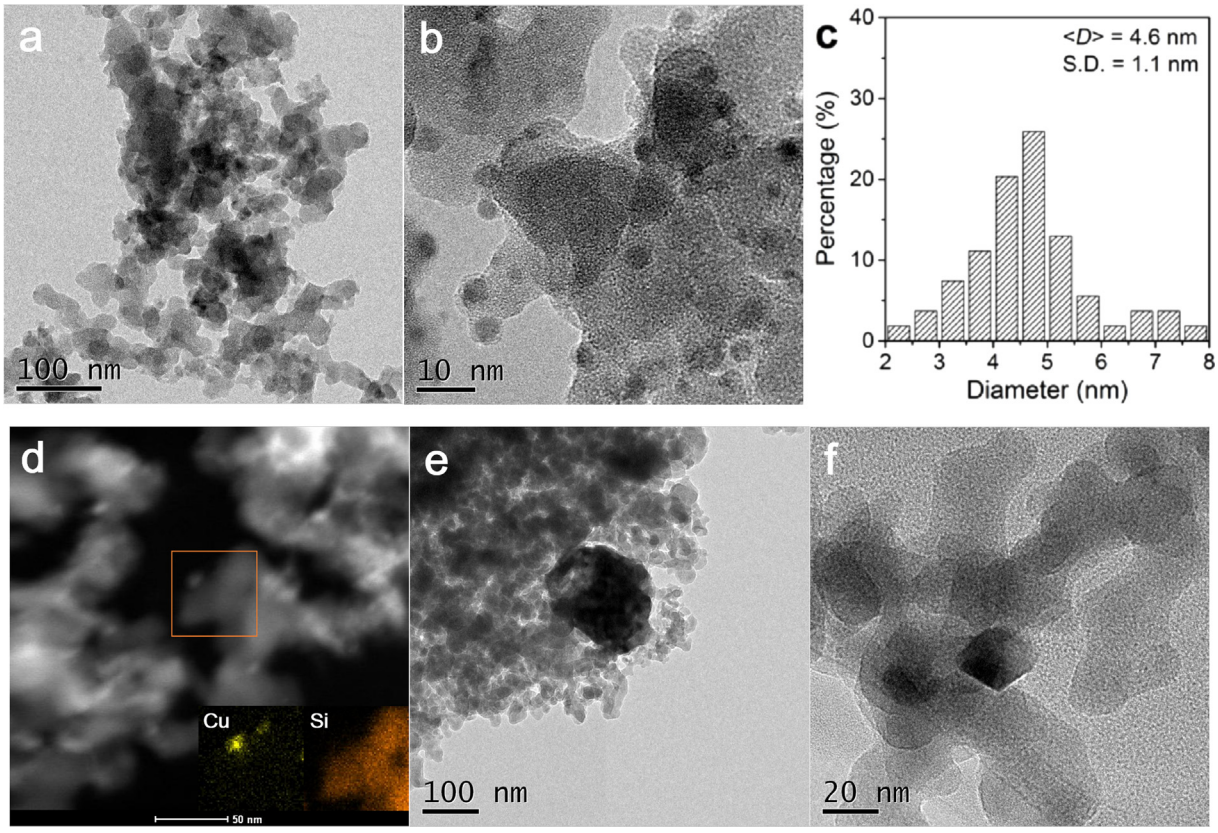


**Fig. 8.** TEM images (a, b, e, f) and the related particle-size histogram for copper species (c) and STEM-EDS mapping results (d) of used copper–silicon nitride catalysts: (a–d) 10Cu/$Si_3N_4$-400; (e, f) 10Cu/$Si_3N_4$-800.

Fig. 9a displays the XANES profiles of used catalysts. With the help of various standards (Cu foil for $Cu^0$, $Cu_2O$ for $Cu^+$, and CuO for $Cu^{2+}$), we have determined their oxidation states as Cu(I) after the selective oxidation of propene. The related EXAFS fitting results (see Fig. 9b and Table 4) show that all the investigated samples after the 325 °C reaction contained the Cu—O ($R$ = 1.87 Å) first shell and the Cu—Cu ($R$ = 3.00 Å) second shell of $Cu_2O$.

Therefore, on the basis of the TEM, XRD, and XANES/EXAFS results, we found that the $Cu_2O$-like species were generated during the hydrogen pretreatment followed by the selective propene oxidation process over the studied copper–silicon nitride catalysts.

### 3.4. Identification of active sites

To investigate the structural evolution of copper species under the activation and reaction conditions and further determine the active species in acrolein formation via selective oxidation of propene, we performed in situ *X*RD measurements on different copper–silicon nitride catalysts. For 10Cu/$Si_3N_4$-400 (see Fig. 10a), the tested sample underwent a temperature-rising reduction process (5% $H_2$/Ar) followed by a 320-min reaction under a propene and oxygen mixture (molar ratio 1:1). No diffraction peaks were observed until the reduction temperature rose to 300 °C, where the characteristic peak of Cu(1 1 1) at 43.0° appeared. This implies that the copper oxide species can be reduced to metallic copper at 300 °C, which was in accord with the $H_2$ TPR results (Fig. S1 and Table 1). Moreover, the Cu(1 1 1) peak remained unchanged when cooled to 30 °C or under other atmospheres (He or $C_3H_6$ + $O_2$). The selective propene oxidation reaction was conducted after the gas was switched to a mixture of $C_3H_6$ and $O_2$ and warmed to 325 °C, where the Cu(1 1 1) peak disappeared and a broader diffraction peak at ca. 36.4° of $Cu_2O$ (1 1 1) was generated immediately, accompanied by a very weak $Cu_2O$ (2 0 0) diffraction peak with slowly increased diffraction intensity during the following reaction process (320 min). This is probably owing to the higher space velocity (160,000 $cm^3 \cdot h^{-1} \cdot g_{cat}^{-1}$) in the in situ XRD experiment than that of the ex situ sample used in the catalytic reaction (30,000 $cm^3 \cdot h^{-1} \cdot g_{cat}^{-1}$). The combination of in situ (Fig. 10a) and ex situ XRD data (Fig. 7a) suggested that the small copper species underwent an evolution of Cu(II) → Cu(0) → Cu(I), and the cuprous oxide species were not overoxidized to copper oxide species in the reaction atmosphere at 325 °C.

The structural transformation was more obvious on 10Cu/$Si_3N_4$-800 than on 10Cu/$Si_3N_4$-400 under the same testing conditions. As shown in Fig. 10b, a very sharp characteristic peak of Cu(1 1 1) was detected at 43.0°, together with two weak diffraction peaks of Cu (0 0 2) and Cu(0 2 2) at 50.1° and 73.6°. All the peaks of CuO vanished after the sample was reduced at 300 °C, indicating that the highly crystallized copper oxide species can be reduced to metallic copper at 300 °C. Furthermore, once the sample reacted at 325 °C in the mixture of $C_3H_6$ and $O_2$, the diffraction peaks of $Cu_2O$ (1 1 1), (2 0 0), (2 2 0), and (3 1 1) appeared. At the same time, the Cu(1 1 1) peak was weakened and soon disappeared. No other CuO diffraction peaks were found even after 320 min of reaction, which was consistent with the ex situ XRD results (Fig. 7a). Therefore, the larger $Cu_2O$ species in 10Cu/$Si_3N_4$-800 is of crucial importance for the acrolein formation.

It was reported that the high-temperature treatment of Cu species on nitrogen-containing material might result in an atomically dispersed copper species, which has exhibited significant activity for the oxygen reduction reaction [67]. To verify the possibility in our system, 10Cu/$Si_3N_4$-800 was leached with 5% aq. HCl for 4 h to remove the weakly bound CuO particles and to compare the reactivity before and after leaching. It can be clearly seen that

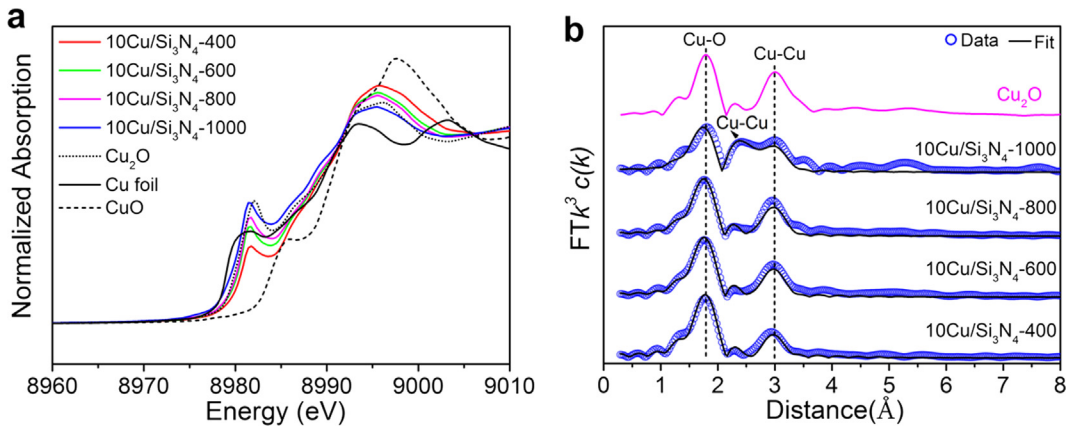


**Fig. 9.** Cu *K*-edge XANES profiles (a) and EXAFS fitting results in *R* space (b) of used copper–silicon nitride catalysts.

**Table 4**
Cu *K*-edge EXAFS fitting results (*R*: distance; CN: coordination number; $\sigma^2$: Debye–Waller factor[a]; $\triangle E_0$: inner potential correction[b]) of 325 °C used catalysts.

| Sample | Cu—O | | Cu—Cu | | Cu—Cu | |
|---|---|---|---|---|---|---|
| | *R* (Å) | CN | *R* (Å) | CN | *R* (Å) | CN |
| $Cu_2O$ | 1.849 | 2 | 3.019 | 12 | | |
| 10Cu/$Si_3N_4$-400 | 1.90 ± 0.01 | 2.6 ± 0.2 | 3.00 ± 0.02 | 6.4 ± 1.2 | – | – |
| 10Cu/$Si_3N_6$-600 | 1.87 ± 0.01 | 2.4 ± 0.2 | 3.01 ± 0.01 | 8.6 ± 1.3 | – | – |
| 10Cu/$Si_3N_4$-800 | 1.87 ± 0.01 | 2.2 ± 0.2 | 3.01 ± 0.01 | 8.9 ± 1.3 | – | – |
| 10Cu/$Si_3N_4$-1000 | 1.85 ± 0.01 | 1.7 ± 0.2 | 2.99 ± 0.02 | 8.0 ± 2.0 | 2.59 ± 0.04 | 2.3 ± 1.0 |

[a] $\sigma^2$ = 0.0046 Å$^2$ (Cu—O) or 0.0203 Å$^2$ (Cu—Cu) for all analyzed samples.
[b] $\Delta E_0$ = 10.8 eV for all analyzed samples.

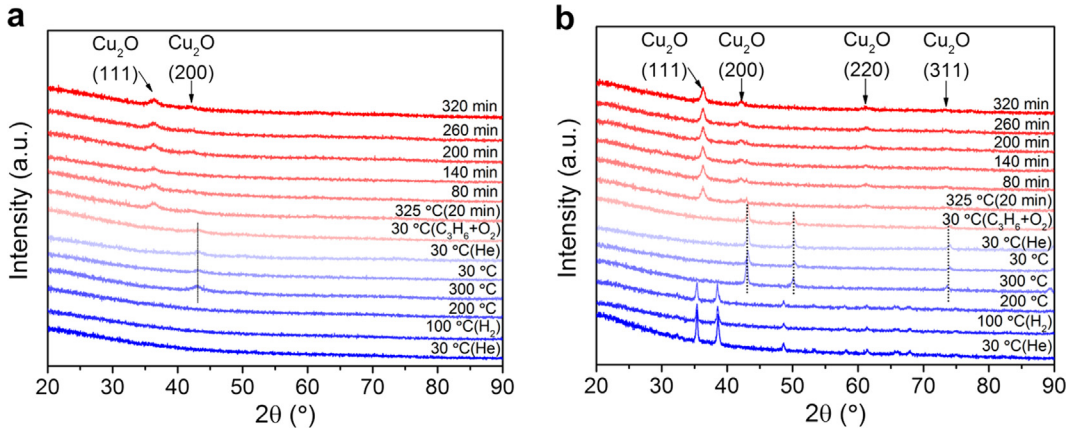


**Fig. 10.** In situ XRD patterns of (a) 10Cu/$Si_3N_4$-400 and (b) 10Cu/$Si_3N_4$-800 under $H_2$ reduction at different temperatures, which were then reacted at 325 °C for 320 min.

the large CuO species was effectively removed (Fig. S16), and the rest of the highly dispersed copper species exhibited extremely poor catalytic activity with ~1% propene conversion over this reaction (Fig. S17), demonstrating that higher reactivity on 10Cu/$Si_3N_4$-800 indeed originated from larger $Cu_2O$ species. Furthermore, commercial bulky $Cu_2O$ particles (~35 nm, 10 wt%) were physically mixed with a silicon nitride material with a copper dispersion of 14.6%, namely *b*-$Cu_2O$/$Si_3N_4$ (Fig. S18 and S19). When reacted at 325 °C, the sample exhibited an acrolein selectivity of 65.4% and a very low propene conversion of only 4.8% (Fig. S20), resulting in a TOF value of 8.4 $h^{-1}$, almost one order of magnitude lower than the 10Cu/$Si_3N_4$-800 catalyst reacted under the same conditions, indicating that the silicon nitride is of crucial importance for fabricating highly active catalysts and the interaction between the metal and support in 10Cu/$Si_3N_4$-800 greatly affected the reactivity of the catalyst. Combining this with the in situ XRD results (Fig. 10), we can conclude that 10Cu/$Si_3N_4$-800 with larger $Cu_2O$ supported on the thermally stable silicon nitride is more active than 10Cu/$Si_3N_4$-400 with smaller $Cu_2O$ for the reaction of selective propene oxidation to acrolein at a relatively higher reaction temperature of 325 °C.

Besides the active sites, the instantaneous surface reaction remarkably influenced their catalytic behaviors. Hence, we performed the temperature-programmed surface reaction (TPSR) over copper–silicon nitride catalysts. $CO_2$ and acrolein as two main products of this reaction were purposely monitored. As shown in Fig. 11a, $CO_2$ started to react at nearly 175 °C over 10Cu/$Si_3N_4$-400, but above 200 °C over 10Cu/$Si_3N_4$-800 (Fig. 11b), indicating that a higher reaction temperature was required for the larger copper species, which was in accordance with the apparent activation

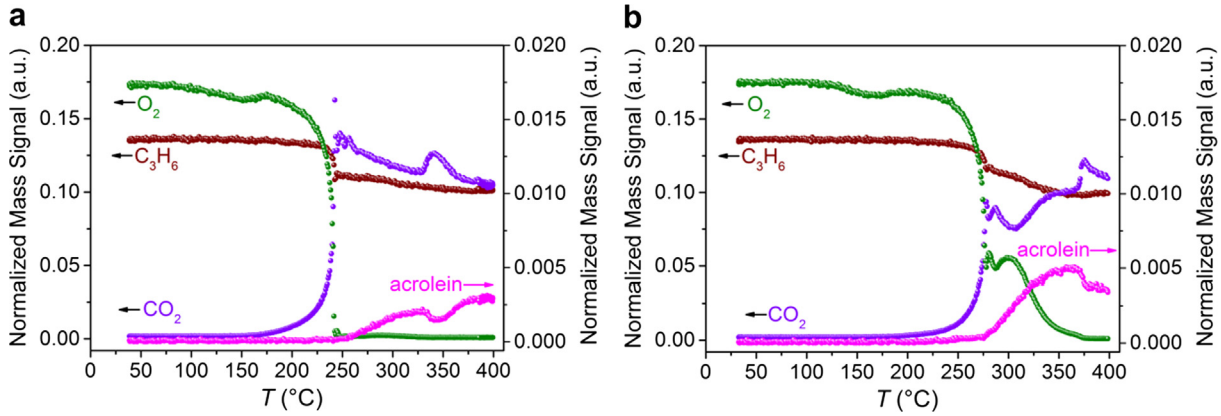


**Fig. 11.** Temperature-programmed surface reaction (TPSR) results for (a) 10Cu/$Si_3N_4$-400 and (b) 10Cu/$Si_3N_4$-800, which were detected by $C_3H_5$ ($m/z$ = 41), $O_2$($m/z$ = 32), acrolein ($m/z$ = 56), and $CO_2$ ($m/z$ = 44). Reaction conditions: 100 mg catalyst, $C_3H_6$:$O_2$:$N_2$/Ar = 5:5:90, 50 mL·min$^{-1}$.

energy results (Fig. 5f). Furthermore, the $CO_2$ amounts of these two samples increased sharply with the reaction temperature until another product (acrolein) was generated. Also, 10Cu/$Si_3N_4$-400 produced a significantly larger amount of $CO_2$ than 10Cu/$Si_3N_4$-800, associated with the surface structure of this catalyst. The main products, including $CO_2$ and acrolein, were clearly observed, and the acrolein intensity of 10Cu/$Si_3N_4$-800 at 325 °C was greater than that of 10Cu/$Si_3N_4$-400, which may result in completely different selectivity of acrolein.

Furthermore, we applied CO TPR tests to detect the properties of surface oxygen or hydroxyls over copper–silicon nitride catalysts [68,69]. To mimic the structural evolution during reaction pretreatment, hydrogen reduction at 300 °C was used to activate the catalyst. For $Si_3N_4$ in Fig. S21a, no $CO_2$ or $H_2O$ signals were detected, confirming that no reaction between the hydroxyls on the pure $Si_3N_4$ support and the CO gas happened. So the generation of $H_2$ and $CO_2$ in Fig. 12 and Fig. S21b during CO TPR could be attributed to surface hydroxyls activated by metal (Cu) to form Cu—OH species after the reduction pretreatment step via the reaction of $CO + 2OH^- \rightarrow CO_2\uparrow + H_2\uparrow + O^{2-}$ with the stoichiometric ratio of ~1:1 for 10Cu/$Si_3N_4$-800 and 10Cu/$Si_3N_4$-400 [68]. The amounts of $CO_2$ and $H_2$ decreased with the calcination temperature and show the order 10Cu/$Si_3N_4$-400 > 10Cu/$Si_3N_4$-600 > 10Cu/$Si_3N_4$-800, implying that the number of Cu—OH species can be greatly tuned by selecting the appropriate calcination temperature. Meanwhile, we applied the in situ DRIFTS measurements to detect the hydroxyls on the copper–silicon nitride catalysts after reduction at 300 °C for 30 min. As shown in Fig. S22, the vibration peaks corresponding to terminal O—H species and Si—O asymmetric stretching vibrations can be observed at 3735, 1250, and 1125 cm$^{-1}$ for 10Cu/$Si_3N_4$-400 and 10Cu/$Si_3N_4$-800. This result verified the formation of terminal Si—OH species, which was favored in photocatalytic reactions [70-72]. In addition, the red shift of hydroxyls in DRIFTS was observed for the copper–silicon nitride catalysts, if they were compared with the pure $Si_3N_4$. This indicates that a strong interaction between copper and silicon nitride formed during the deposition and the following calcination process, leading to enhanced catalytic activity for selective propene oxidation to produce acrolein [73]. On the other hand, the Cu—OH band at nearly 3538 cm$^{-1}$ was not observed in DRIFTS, probably because of the limited amount of Cu—OH on the surface of 10Cu/$Si_3N_4$-400 and 10Cu/$Si_3N_4$-800 [74].

More importantly, the rates of $CO_2$ production determined by TPSR over both 10Cu/$Si_3N_4$-400 and 10Cu/$Si_3N_4$-800 were closely proportional to the amounts of surface hydroxyls (Fig. S23). For the catalytic performance of 10Cu/$Si_3N_4$-400 in Fig. S8a, it is interesting that the selectivity for acrolein was increased linearly from 39 to 74% in the initial 200 min and then became stable, while the selectivity for $CO_2$ decreased rapidly from 58 to 23% at the same time. This indicates that the surface Cu—OH can induce the reaction between $C_3H_6$ and $O_2$ to form $CO_2$ preferentially at the beginning of the oxidation reaction, and the acrolein product increases as $CO_2$ decreases with the consumption of Cu—OH during the sequential period. For 10Cu/$Si_3N_4$-600, the induction time was shortened to 150 min (Fig. S8c), while for 10Cu/$Si_3N_4$-800 with less Cu—OH in Fig. S6b, the selectivity for acrolein and $CO_2$ was almost

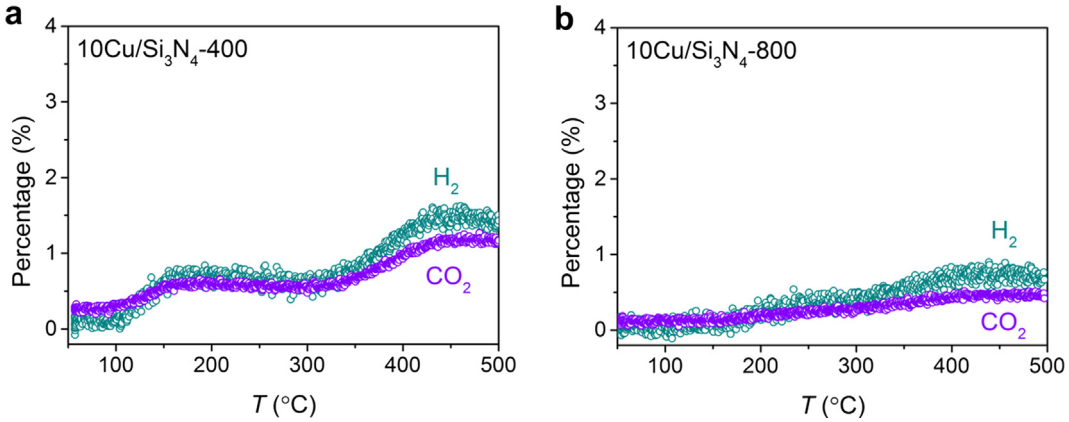


**Fig. 12.** CO TPR profiles of (a) 10Cu/$Si_3N_4$-400 and (b) 10Cu/$Si_3N_4$-800 detected by $H_2$ ($m/z$ = 2) and $CO_2$ ($m/z$ = 44).

unchanged in the whole reaction process. These catalysts can be ranked in terms of acrolein selectivity: 10Cu/$Si_3N_4$-400 < 10Cu/$Si_3N_4$-600 < 10Cu/$Si_3N_4$-800. Therefore, we can obtain the conclusion that the silicon nitride material was vital in constructing the highly active copper-based catalyst, and the higher calcination temperature in preparation can eliminate the surface Cu-OH species, and thus lower the selectivity for $CO_2$ and simultaneously improve the acrolein selectivity.

## 4. Conclusions

In summary, an amorphous silicon nitride was selected to immobilize a series of copper oxides through a deposition–precipitation approach. The fresh catalysts calcined at different temperatures exhibited completely different catalytic performance for selective propene oxidation to acrolein. The as-synthesized 10Cu/$Si_3N_4$-800 with good structural stability showed superior catalytic activity with 24.0% propene conversion and 86.2% acrolein selectivity at 325 °C, attaining an acrolein formation rate value of 136.9 $mmol{\cdot}h^{-1}g_{Cu}^{-1}$ or 12.7 $mmol{\cdot}h^{-1}g_{cat}^{-1}$ and a turnover frequency (TOF) of 80.6 $h^{-1}$. With the aid of multiple characterization means, we have identified that the larger $Cu_2O$ species and the interaction between the active species and the silicon nitride with a partially oxidized surface account for the origin of a highly effective reaction between $C_3H_6$ and $O_2$ to form acrolein at 325 °C. Furthermore, we have verified that the surface Cu—OH species favor the formation of $CO_2$ during the initial reaction period, displaying an induction time. By optimizing the air-calcination temperature, the activity of copper–silicon nitride catalysts can be improved through the elimination of surface Cu—OH species. The unique thermal stability of silicon nitride is of crucial importance for the fabrication of highly active catalysts reacted at higher temperatures.

## Acknowledgements

Financial support from the National Science Foundation of China (Grant 21773288) and the National Key Basic Research Program of China (2017YFA0403402) is acknowledged.

## Appendix A. Supplementary material

Supplementary data to this article can be found online at https://doi.org/10.1016/j.jcat.2019.09.019.

## References

[1] J.L. Callahan, R.K. Grasselli, E.C. Milberger, H.A. Strecker, Oxidation and ammoxidation of propylene over bismuth molybdate catalyst, Ind. Eng. Chem. Prod. Res. Dev. 9 (1970) 134–142.
[2] A.-R. Leeds, Xylidine-acrolein, J. Am. Chem. Soc. 5 (1883) 1–2.
[3] T. Kano, T. Hashimoto, K. Maruoka, Asymmetric 1,3-dipolar cycloaddition reaction of nitrones and acrolein with a bis-titanium catalyst as chiral lewis acid, J. Am. Chem. Soc. 127 (2005) 11926–11927.
[4] K.-H. Dostert, C.P. O'Brien, F. Ivars-Barceló, S. Schauermann, H.-J. Freund, Spectators control selectivity in surface chemistry: acrolein partial hydrogenation over Pd, J. Am. Chem. Soc. 137 (2015) 13496–13502.
[5] Z. Xi, N. Zhou, Y. Sun, K. Li, Reaction-controlled phase-transfer catalysis for propylene epoxidation to propylene oxide, Science 292 (2001) 1139–1141.
[6] B.-K. Min, C.-M. Friend, Heterogeneous gold-based catalysis for green chemistry: low-temperature CO oxidation and propene oxidation, Chem. Rev. 107 (2007) 2709–2724.
[7] Y. Lei, F. Mehmood, S. Lee, J. Greeley, B. Lee, S. Seifert, R.-E. Winans, J.-W. Elam, R.-J. Meyer, P.-C. Redfern, D. Teschner, R. Schlögl, M.-J. Pellin, L.-A. Curtiss, S. Vajda, Increased silver activity for direct propylene epoxidation via subnanometer size effects, Science 328 (2010) 224–228.
[8] S.J. Khatib, S.T. Oyama, Direct oxidation of propylene to propylene oxide with molecular oxygen: a review, Catal. Rev. 57 (2015) 306–344.
[9] D.M. Driscoll, W. Tang, S.P. Burrows, D.A. Panayotov, M. Neurock, M. McEntee, J.R. Morris, Binding sites, geometry, and energetics of propene at nanoparticulate Au/$TiO_2$, J. Phys. Chem. C 121 (2017) 1683–1689.
[10] J. Teržan, P. Djinović, J. Zavašnik, I. Arčon, G. Žerjav, M. Spreitzer, A. Pintar, Alkali and earth alkali modified $CuO_x/SiO_2$ catalysts for propylene partial oxidation: what determines the selectivity, Appl. Catal. B Environ. 237 (2018) 214–227.
[11] Y.-H. Han, W. Ueda, Y. Moro-Oka, Lattice oxide ion-transfer effect demonstrated in the selective oxidation of propene over silica-supported bismuth molybdate catalysts, Appl. Catal. A Gen. 176 (1999) 11–16.
[12] L.J. Deiner, J.G. Serafin, C.M. Friend, S.G. Weller, J.A. Levinson, R.E. Palmer, Insight into the partial oxidation of propene: the reactions of 2-propen-1-ol on clean and O-covered Mo(110), J. Am. Chem. Soc. 125 (2003) 13252–13257.
[13] S.R.G. Carrazán, C. Martín, R. Mateos, V. Rives, Influence of the active phase structure Bi-Mo-Ti-O in the selective oxidation of propene, Catal. Today 112 (2006) 121–125.
[14] S. Pudar, J. Oxgaard, K. Chenoweth, A.C.T. van Duin, W.A. Goddard, Mechanism of selective oxidation of propene to acrolein on bismuth molybdates from quantum mechanical calculations, J. Phys. Chem. C 111 (2007) 16405–16415.
[15] A.B. Getsoian, V. Shapovalov, A.T. Bell, DFT+U investigation of propene oxidation over bismuth molybdate: active sites, reaction intermediates, and the role of bismuth, J. Phys. Chem. C 117 (2013) 7123–7137.
[16] A. Nell, A.B. Getsoian, S. Werner, L. Kiwi-Minsker, A.T. Bell, Preparation and characterization of high-surface-area $Bi_{(1-x)/3}V_{1-x}Mo_xO_4$ catalysts, Langmuir 30 (2014) 873–880.
[17] A.B. Getsoian, Z. Zhai, A.T. Bell, Band-gap energy as a descriptor of catalytic activity for propene oxidation over mixed metal oxide catalysts, J. Am. Chem. Soc. 136 (2014) 13684–13697.
[18] B. Farin, A.H.A.M. Videla, S. Specchia, E.M. Gaigneaux, Gaigneaux, Bismuth molybdates prepared by solution combustion synthesis for the partial oxidation of propene, Catal. Today 257 (2015) 11–17.
[19] L. Bui, R. Chakrabarti, A. Bhan, Mechanistic origins of unselective oxidation products in the conversion of propylene to acrolein on $Bi_2Mo_3O_{12}$, ACS Catal. 6 (2016) 6567–6580.
[20] Z. Zhai, M. Wütschert, R.B. Licht, A.T. Bell, Effects of catalyst crystal structure on the oxidation of propene to acrolein, Catal. Today 261 (2016) 146–153.
[21] G.I. Panov, E.V. Starokon, M.V. Parfenov, B. Wei, V.I. Sobolev, L.V. Pirutko, Quasi-catalytic identification of intermediates in the oxidation of propene to acrolein over a multicomponent Bi-Mo catalyst, ACS Catal. 8 (2018) 1173–1177.
[22] G.I. Panov, M.V. Parfenov, E.V. Starokon, A.S. Kharitonov, Investigation of propene oxidation to acrolein by the method of ultralow conversion: a new mechanism of the reaction, J. Catal. 368 (2018) 315–323.
[23] C.R. Adams, T.J. Jennings, Investigation of the mechanism of catalytic oxidation of propylene to acrolein and acrylonitrile, J. Catal. 2 (1963) 63–68.
[24] C.R. Adams, T.J. Jennings, Mechanism studies of the catalytic oxidation of propylene, J. Catal. 3 (1964) 549–558.
[25] K.H. Schulz, D.F. Cox, Surface reactions of acrolein and propionaldehyde on cuprous oxide(100): nonselective oxidation and enolate-mediated side reactions to C3 products, J. Phys. Chem. 97 (1993) 3555–3564.
[26] J.B. Reitz, E.I. Solomon, Propylene oxidation on copper oxide surfaces: electronic and geometric contributions to reactivity and selectivity, J. Am. Chem. Soc. 120 (1998) 11467–11478.
[27] O.P.H. Vaughan, G. Kyriakou, N. Macleod, M. Tikhov, R.M. Lambert, Copper as a selective catalyst for the epoxidation of propene, J. Catal. 236 (2005) 401–404.
[28] W. Su, S. Wang, P. Ying, Z. Feng, C. Li, A molecular insight into propylene epoxidation on Cu/$SiO_2$ catalysts using $O_2$ as oxidant, J. Catal. 268 (2009) 165–174.
[29] H. Tüysüz, J.L. Galilea, Highly diluted copper in a silica matrix as active catalyst for propylene oxidation to acrolein, Catal. Lett. 131 (2009) 49–53.
[30] K.L. Bøyesen, K. Mathisen, Exposing the synergistic effect between copper and vanadium in AlPO-5 during the selective oxidation of propene, Catal. Today 229 (2014) 14–22.
[31] C.-H. Liu, N.-C. Lai, J.-F. Lee, C.-S. Chen, C.-M. Yang, SBA-15-supported highly dispersed copper catalysts: vacuum-thermal preparation and catalytic studies in propylene partial oxidation to acrolein, J. Catal. 316 (2014) 231–239.
[32] W. Song, D.M.P. Ferrandez, L. van Haandel, P. Liu, T.A. Nijhuis, E.J.M. Hensen, Selective propylene oxidation to acrolein by gold dispersed on $MgCuCr_2O_4$ spinel, ACS Catal. 5 (2015) 1100–1111.
[33] D. Düzenli, D.O. Atmaca, M.G. Gezer, I. Onal, A density functional theory study of partial oxidation of propylene on $Cu_2O$(001) and CuO(001) surfaces, Appl. Surf. Sci. 355 (2015) 660–666.
[34] K.L. Bøyesen, T. Kristiansen, K. Mathisen, Dynamic redox properties of vanadium and copper in microporous supports during the selective oxidation of propene, Catal. Today 254 (2015) 21–28.
[35] N.-C. Lai, M.-C. Tsai, C.-H. Liu, C.-S. Chen, C.-M. Yang, Efficient selective oxidation of propylene by dioxygen on mesoporous-silica-nanoparticle-supported nanosized copper, J. Catal. 365 (2018) 411–419.
[36] X. Deng, B.K. Min, X. Liu, C.M. Friend, Partial oxidation of propene on oxygen-covered Au(111), J. Phys. Chem. B 110 (2006) 15982–15987.
[37] Y. Cui, Y. Xia, J. Zhao, L. Li, T. Fu, N. Xue, L. Peng, X. Guo, W. Ding, Super high selectivity of acrolein in oxidation of propene on molybdenum promoted hierarchical assembly of bismuth tungstate nanoflakes, Appl. Catal. A Gen. 482 (2014) 179–188.
[38] D.M.P. Ferrandez, I.H. Fernandez, M.P.G. Teley, M.H.J.M. de Croon, J.C. Schouten, T.A. Nijhuis, Kinetic study of the selective oxidation of propene with $O_2$ over Au-Ti catalysts in the presence of water, J. Catal. 330 (2015) 396–405.
[39] F. Liao, Y. Huang, J. Ge, W. Zheng, K. Tedsree, P. Collier, X. Hong, S.C. Tsang, Morphology-dependent interactions of ZnO with Cu nanoparticles at the

materials' interface in selective hydrogenation of $CO_2$ to $CH_3OH$, Angew. Chem. Int. Ed. 50 (2011) 2162–2165.
[40] F. Liao, Z. Zeng, C. Eley, Q. Lu, X. Hong, S.C.E. Tsang, Electronic modulation of a copper/zinc oxide catalyst by a heterojunction for selective hydrogenation of carbon dioxide to methanol, Angew. Chem. Int. Ed. 51 (2012) 5832–5836.
[41] C. Xu, G. Chen, Y. Zhao, P. Liu, X. Duan, L. Gu, G. Fu, Y. Yuan, N. Zheng, Interfacing with silica boosts the catalysis of copper, Nat. Commun. 9 (2018) 1–10.
[42] A.M. Harzandi, J.N. Tiwari, H.S. Lee, H. Jeon, W.J. Cho, G. Lee, J. Baik, J.H. Kwak, K.S. Kim, Efficient CO oxidation by 50-facet $Cu_2O$ nanocrystals coated with CuO nanoparticles, ACS Appl. Mater. Interfaces 9 (2017) 2495–2499.
[43] B. Huang, H. Kobayashi, T. Yamamoto, S. Matsumura, Y. Nishida, K. Sato, K. Nagaoka, S. Kawaguchi, Y. Kubota, Solid-solution alloying of immiscible Ru and Cu with enhanced CO oxidation activity, J. Am. Chem. Soc. 139 (2017) 4643–4646.
[44] J.A. Rodriguez, J. Graciani, J. Evans, J.B. Park, F. Yang, D. Stacchiola, S.D. Senanayake, S. Ma, M. Pérez, P. Liu, J.F. Sanz, J. Hrbek, Water-gas shift reaction on a highly active inverse $CeO_x$/Cu(111) catalyst: unique role of ceria nanoparticles, Angew. Chem. Int. Ed. 48 (2009) 8047–8050.
[45] Z. Zhang, S.-S. Wang, R. Song, T. Cao, L. Luo, X. Chen, Y. Gao, J. Lu, W.-X. Li, W. Huang, The most active Cu facet for low-temperature water gas shift reaction, Nat. Commun. 8 (2017) 1–10.
[46] M.D. Marcinkowski, C.J. Murphy, M.L. Liriano, N.A. Wasio, F.R. Lucci, E.C.H. Sykes, Microscopic view of the active sites for selective dehydrogenation of formic acid on Cu(111), ACS Catal. 5 (2015) 7371–7378.
[47] M. Tamura, T. Kitanaka, Y. Nakagawa, K. Tomishige, Cu sub-nanoparticles on $Cu/CeO_2$ as an effective catalyst for methanol synthesis from organic carbonate by hydrogenation, ACS Catal. 6 (2016) 376–380.
[48] H. Yang, Y. Chen, X. Cui, G. Wang, Y. Cen, T. Deng, W. Yan, J. Gao, S. Zhu, U. Olsbye, J. Wang, W. Fan, A highly stable copper-based catalyst for clarifying the catalytic roles of $Cu^0$ and $Cu^+$ species in methanol dehydrogenation, Angew. Chem. Int. Ed. 57 (2018) 1836–1840.
[49] J. Yu, L. Kevan, Effects of reoxidation and water vapor on selective partial oxidation of propylene to acrolein in copper(II)-exchanged X and Y zeolites, J. Phys. Chem. 95 (1991) 6648–6653.
[50] J. He, Q. Zhai, Q. Zhang, W. Deng, Y. Wang, Active site and reaction mechanism for the epoxidation of propylene by oxygen over $CuO_x/SiO_2$ catalysts with and without $Cs^+$ modification, J. Catal. 299 (2013) 53–66.
[51] M. Tonelli, M. Aouine, L. Massin, V.B. Bacab, J.M.M. Millet, Selective oxidation of propene to acrolein on FeMoTeO catalysts: determination of active phase and enhancement of catalytic activity and stability, Catal. Sci. Technol. 7 (2017) 4629–4639.
[52] L. Liu, X.P. Ye, J.J. Bozell, A comparative review of petroleum-based and bio-based acrolein production, ChemSusChem 5 (2012) 1162–1180.
[53] H.-C. Wu, C.-S. Chen, C.-M. Yang, M.-C. Tsai, J.-F. Lee, Decomposition of large Cu crystals into ultrasmall particles using chemical vapor deposition and their application in selective propylene oxidation, ACS Appl. Mater. Interfaces 10 (2018) 38547–38557.
[54] C.L. Bracey, A.F. Carley, J.K. Edwards, P.R. Ellis, G.J. Hutchings, Understanding the effect of thermal treatments on the structure of $CuAu/SiO_2$ catalysts and their performance in propene oxidation, Catal. Sci. Technol. 1 (2011) 76–85.
[55] S. Belin, C.L. Bracey, V. Briois, P.R. Ellis, G.J. Hutchings, T.I. Hyde, G. Sankar, $CuAu/SiO_2$ catalysts for the selective oxidation of propene to acrolein: the impact of catalyst preparation variables on material structure and catalytic performance, Catal. Sci. Technol. 3 (2013) 2944–2957.
[56] J. Lu, M. Luo, H. Lei, X. Bao, C. Li, Epoxidation of propylene on NaCl-modified VCe1−x Cux oxide catalysts with direct molecular oxygen as the oxidant, J. Catal. 211 (2002) 552–555.
[57] X. Yang, S. Kattel, K. Xiong, K. Mudiyanselage, S. Rykov, S.D. Senanayake, J.A. Rodriguez, P. Liu, D.J. Stacchiola, J.G. Chen, Direct epoxidation of propylene over stabilized $Cu^+$ surface sites on titanium-modified $Cu_2O$, Angew. Chem. Int. Ed. 54 (2015) 11946–11951.
[58] R. Xia, Y. Zhang, Q. Zhu, J. Qian, Q. Dong, F. Li, Surface modification of nano-sized silicon nitride with BA-MAA-AN tercopolymer, J. Appl. Polym. Sci. 107 (2008) 562–570.
[59] S. Lojanová, P. Tatarko, Z. Chlup, M. Hnatko, J. Dusza, Z. Lenčéš, P. Šajgalík, Rare-earth element doped SiN/SiC micro/nano-composites-RT and HT mechanical properties, J. Eur. Ceram. Soc. 30 (2010) 1931–1944.
[60] J. Hu, L. Fang, P.-W. Zhong, A.-Q. Tang, B. Yin, Y. Li, Preparation and properties of Ni-Co-P/nano-sized $Si_3N_4$ electroless composite coatings, Surf. Interface Anal. 44 (2012) 450–455.
[61] J. Liu, Y. Gu, F. Li, F. Li, L. Lu, H. Zhang, S. Zhang, Catalytic nitridation preparation of high-performance $Si_3N_4$(w)-SiC composite using $Fe_2O_3$ nano-particle catalyst: experimental and DFT studies, J. Eur. Ceram. Soc. 37 (2017) 4467–4474.
[62] Z. Hu, W. Huo, T. Zhu, J. Liu, Z. Xie, Preparation of -$Si_3N_4$ nanorods assembled nanobelts by crystallizing amorphous $Si_3N_4$ powders, Physica E Low-Dimens. Syst. Nanostruct. 112 (2019) 137–141.
[63] M. Biesuz, P. Bettotti, S. Signorini, M. Bortolotti, R. Campostrini, B. Bahri, O. Ersen, G. Speranza, A. Lale, S. Bernard, G.D. Sorarù, First synthesis of silicon nanocrystals in amorphous silicon nitride from a preceramic polymer, Nanotechnology 30 (2019) 255601.
[64] J.I. Langford, Powder pattern programs, J. Appl. Crystallogr. 4 (1971) 259–260.
[65] J.I. Langford, The accuracy of cell dimensions determined by Cohen's method of least squares and the systematic indexing of powder data, J. Appl. Crystallogr. 6 (1973) 190–196.
[66] Z.-Q. Wang, Z.-N. Xu, S.-Y. Peng, M.-J. Zhang, G. Lu, Q.-S. Chen, Y. Chen, G.-C. Guo, High-performance and long-lived $Cu/SiO_2$ nanocatalyst for $CO_2$ hydrogenation, ACS Catal. 5 (2015) 4255–4259.
[67] F. Li, G.-F. Han, H.-J. Noh, S.-J. Kim, Y. Lu, H.Y. Jeong, Z. Fu, J.-B. Baek, Boosting oxygen reduction catalysis with abundant copper single atom active sites, Energy Environ. Sci. 11 (2018) 2263–2269.
[68] Y. Wang, Q. Yuan, Q. Zhang, W. Deng, Characterizations of unsupported and supported rhodium-iron phosphate catalysts effective for oxidative carbonylation of methane, J. Phys. Chem. C 111 (2007) 2044–2053.
[69] Q. Fu, H. Saltsburg, M. Flytzani-Stephanopoulos, Active nonmetallic Au and Pt species on ceria-based water-gas shift catalysts, Science 301 (2003) 935–938.
[70] H. Yoshida, C. Murata, T. Hattori, Screening study of silica-supported catalysts for photoepoxidation of propene by molecular oxygen, J. Catal. 194 (2000) 364–372.
[71] L. Yuliati, M. Tsubota, A. Satsuma, H. Itoh, H. Yoshida, Photoactive sites on pure silica materials for nonoxidative direct methane coupling, J. Catal. 238 (2006) 214–220.
[72] W.H. Saputera, H.A. Tahini, E.C. Lovell, T.H. Tan, A. Rawal, K.-F. Aguey-Zinsou, D. Friedmann, S.C. Smith, R. Amal, J. Scott, Cooperative defect-enriched $SiO_2$ for oxygen activation and organic dehydrogenation, J. Catal. 376 (2019) 168–179.
[73] J. Joseph, E.D. Jemmis, Red-, blue-, or no-shift in hydrogen bonds: a unified explanation, J. Am. Chem. Soc. 129 (2007) 4620–4632.
[74] M.D. Driessen, V.H. Grassian, Oxidation of methyl to methoxy on oxidized Cu/$SiO_2$, J. Phys. Chem. 99 (1995) 16519–16522.